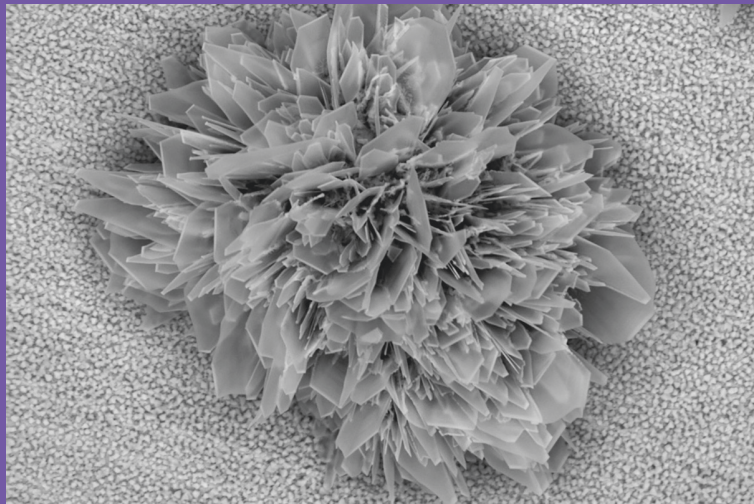


Corrosion mechanisms of the heat recovery boiler of copper flash smelting

Hanna Viitala



Corrosion mechanisms of the heat recovery boiler of copper flash smelting

Hanna Viitala

A doctoral dissertation completed for the degree of Doctor of Science (Technology) to be defended, with the permission of the Aalto University School of Chemical Engineering, at a public examination held at the lecture hall Ke2 of the school on 7 February 2020 at 12.00.

Aalto University
School of Chemical Engineering
Department of Metallurgical and Chemical Engineering
Thermodynamics of Metallurgical Processes

Supervising professor

Professor Daniel Lindberg, Aalto University, Finland

Thesis advisor

Professor Emeritus Pekka Taskinen, Aalto University, Finland

Preliminary examiners

Professor Rainer Backman, Umeå University, Sweden

Professor Jesper Liske, Chalmers University of Technology, Sweden

Opponent

Dr. Rikard Norling, Swerea - Swedish Research, Sweden

Aalto University publication series

DOCTORAL DISSERTATIONS 16/2020

© 2020 Hanna Viitala

ISBN 978-952-60-8929-4 (printed)

ISBN 978-952-60-8930-0 (pdf)

ISSN 1799-4934 (printed)

ISSN 1799-4942 (pdf)

<http://urn.fi/URN:ISBN:978-952-60-8930-0>

Unigrafia Oy

Helsinki 2020

Finland



Author

Hanna Viitala

Name of the doctoral dissertation

Corrosion mechanisms of the heat recovery boiler of copper flash smelting

Publisher School of Chemical Engineering

Unit Department of Metallurgical and Chemical Engineering

Series Aalto University publication series DOCTORAL DISSERTATIONS 16/2020

Field of research Metallurgy

Manuscript submitted 11 October 2019

Date of the defence 7 February 2020

Permission for public defence granted (date) 18 December 2019

Language English

☐ **Monograph**

☒ **Article dissertation**

☐ **Essay dissertation**

Abstract

The flash smelting process is used widely around the world to extract primary copper. Smelting of sulphidic copper ores produces flue dust containing SO₂-rich exhaust gas, causing corrosion problems in the gas cleaning equipment of the process, especially in the heat recovery boiler. The aim of this thesis was to understand the corrosion mechanisms of the boiler steels and to determine what kind of steel would provide the best corrosion protection. Especially the flue dust causes corrosion problems due to formation of dust accretions on the boiler walls. Within these presence heavy metal chlorides results in formation of molten salt deposits causing rapid corrosion.

In order to understand the corrosion behaviour of the boiler steels, conditions of the heat recovery boiler were simulated in laboratory. Corrosion reactions of carbon steel and three high alloy steels (AISI 304, AISI 316 and Sanicro 28) were studied, focusing on corrosion protection properties of chromium, molybdenum and nickel alloying. In addition, thermogravimetric measurements of oxidation behaviour of a stainless steel (TP347H) with two different grain sizes were studied to determine the effect of grain size on the quality and formation of the steel's protective oxide scale. Melting of the dust accretions was identified as the initiator of series of corrosion reactions between the steels and the environment inside the heat recovery boiler. To verify the possibility of formation of molten salt deposits, phase diagrams of few of the possible chloride systems present in the dust accretions were studied experimentally by equilibration-quenching, scanning electron microscopy and energy-dispersive spectrometry in order to evaluate the melting behaviour of these chlorides. Different binaries of the CuCl-CuCl₂-ZnCl₂-PbCl₂-FeCl₃-FeCl₂-system were optimized using the CALPHAD-method.

In this thesis, a description of the sequence of corrosion reactions is given between steel and the chemical environment of the heat recovery boiler. Understanding the corrosion mechanism of the boiler should help to improve its lifetime by selection of suitable steels or by adjusting the operational parameters. Thus, the effectiveness of copper production can be improved

Keywords Corrosion, Molten Salts, Copper flash smelting, Heat Recovery Boiler

ISBN (printed) 978-952-60-8929-4

ISBN (pdf) 978-952-60-8930-0

ISSN (printed) 1799-4934

ISSN (pdf) 1799-4942

Location of publisher Helsinki

Location of printing Helsinki **Year** 2020

Pages 146

urn <http://urn.fi/URN:ISBN:978-952-60-8930-0>

Tekijä

Hanna Viitala

Väitöskirjan nimi

Terästen korroosiomekanismien määrittäminen kuparin liekkisulatusprosessin lämmöntalteenottokattilan olosuhteissa

Julkaisija Kemian tekniikan korkeakoulu**Yksikkö** Kemian tekniikan ja metallurgian laitos**Sarja** Aalto University publication series DOCTORAL DISSERTATIONS 16/2020**Tutkimusala** Metallurgia**Käsikirjoituksen pvm** 11.10.2019**Väitöspäivä** 07.02.2020**Väittelyluvan myöntämispäivä** 18.12.2019**Kieli** Englanti☐ **Monografia**☒ **Artikkeliväitöskirja**☐ **Esseeväitöskirja****Tiivistelmä**

Liekkisulatus on yleisimpiä maailmanlaajuisessa käytössä olevia kuparintuotantomenetelmiä. Sulfidisten kuparimalmien sulatus tuottaa suuria määriä lentopölyä ja runsaasti rikkidioksidia sisältävää poistokaasua, joka aiheuttaa korroosio-ongelmia liekkisulatusprosessin kaasunpuhdistuslaitteistossa, erityisesti lämmöntalteenottokattilassa. Tämän työn tarkoituksena on selvittää lämmöntalteenottokattilan korroosiomekanismi sekä määrittää minkälainen teräs soveltuu parhaiten kattilan materiaaliksi. Poistokaasun sisältämä lentopöly aiheuttaa erityisesti korroosio-ongelmia, sillä se muodostaa raskasmetallisuoloja sisältäviä kerrostumia kattilan teräspinnoille. Näissä pölykerrostumissa esiintyvät kloridit laskevat pölyn sulamispistettä siten, että kattilan teräpinnoille muodostuu paikoittain suolasulia, joiden alla oleva teräs syöpyy nopeasti.

Lämmöntalteenottokattilan terästen korroosiomekanismin ymmärtämiseksi, kattilan olosuhteita simuloitiin laboratorio-olosuhteissa. Hiiliteräs ja kolme erilaista ruostumatonta terästä (AISI 304, AISI 316 ja Sanicro 28) valittiin näyttemateriaaleiksi, sillä kromi-, molybdeeni- ja nikkeliseostuksen välisiä eroja haluttiin tutkia teräksen korroosionkeston kannalta. Myös teräksen (TP347H) raekoon vaikutusta sen pinnalle muodostuvan, suojaavan oksidikerroksen muodostumiseen ja ominaisuuksiin tutkittiin termogravimetrian avulla. Pölykerrostumien sulamisen todettiin olevan pääasiallinen korroosioaurion mahdollistava tekijä. Suolasulien muodostumisen mahdollisuuden todistamiseksi, joidenkin pölyssä todennäköisesti esiintyvien kloridisysteemien faasitasapainoja mitattiin tasapainotus- sammutus-menetelmällä. Erinäisiä CuCl-CuCl₂-ZnCl₂-PbCl₂-FeCl₃-FeCl₂-systeemin binäärisiä faasitasapainoja optimoitiin CALPHAD-tekniikalla.

Tässä väitöskirjassa kuvataan kuparin liekkisulatusprosessin lämmöntalteenottokattilan korroosiomekanismi. Kattilan terästen ja sen olosuhteiden välisten vuorovaikutusten ymmärtäminen mahdollistaa olosuhteisiin nähden parhaan teräksen valinnan tai mahdollisuuden vaikuttaa kattilassa vallitseviin olosuhteisiin korroosion keston kannalta optimaalisella tavalla. Näin kuparin tuotannon tehokkuutta voidaan parantaa.

Avainsanat Korroosio, Suolasulat, Kuparin liekkisulatus, Lämmöntalteenottokattila**ISBN (painettu)** 978-952-60-8929-4**ISBN (pdf)** 978-952-60-8930-0**ISSN (painettu)** 1799-4934**ISSN (pdf)** 1799-4942**Julkaisupaikka** Helsinki**Painopaikka** Helsinki**Vuosi** 2020**Sivumäärä** 146**urn** <http://urn.fi/URN:ISBN:978-952-60-8930-0>

Preface

The research presented in this doctoral thesis was carried out at Aalto University, School of Chemical Engineering, Department of Chemical and Metallurgical Engineering at the research group of Metallurgical Thermodynamics and Modelling (TDM) during the years 2013 – 2019. This work was funded by Metso Power, Metso Minerals and TEKES (Business Finland) as part of Demapp SHOK program of FIMECC Oy, Steel and Metal Producer's Fund, Eemil Aaltonen Foundation and Walter Ahlström Foundation. All the financing parties supporting this research are highly appreciated.

I would like to express my gratitude to my supervisor, emeritus professor Pekka Taskinen, who introduced me to this research and whose expertise and guidance have been of great value and deeply appreciated. It has been an honour to learn from you and work with you all these years. Special thanks also belong to my supervising professor Daniel Lindberg for all the help and effort in improving the thesis and especially for teaching me thermodynamic modelling. Your patient and kind approach has meant a lot to me.

The research group of Metallurgical Thermodynamics and Modelling has been a lovely place to work and thanks for that belongs to my colleagues. I want to thank my favorite office roommates Markus Aspiala, Pilvi Lamb, professor Rauf Hurman Eric and Lassi Klementtinen for the relaxed and warm atmosphere. I never forget all the adventures together in and out of the lab with Markus Asiapala, Pilvi Lamb, Antti Forsström, Sonja Ottelin, Emmi Ollila, Petteri Halli, Inka Mäkinen, Alexandra Zuhlke, Joseph Hamuyuni, Rui Zhang, Petteri Piskunen and Dmitry Sukhomlinov. My special thanks belongs to my corrosion colleagues Sonja Ottelin and Matti Ottelin for guiding me and helping me to this years long path into the exciting world of corrosion. I would also like to thank my colleagues Niko Hellsten, Katri Avramaa, Fiseha Tesfaye, Imam Santoso, Longgong Xia, Hannu Sippola, professor Ari Jokilaakso and professor Michael Gasik for all the advice, great talks and good time together. Most of all I would like to thank Emmi Ollila, Alexandra Zuhlke and professor Annukka Santasalo-Aarnio for all the emotional support and motivation to carry this research through. I would also like to acknowledge and give my thanks to my nice lunch companions in the Mineral Processing and Recycling group (professor Rodrigo Serna, Ted, Omar, Robert) for all the memorable conversations and great time together. I would also like to thank Lauri Viitala for beginning and sharing this journey with me.

My deepest gratitude belongs to my mom and dad whose loving upbringing and unwavering support has given me an indispensable feeling of safety and acceptance, so that I never needed to be afraid of failing. I am always grateful to my father for giving me the interest in science and for being my best teacher. Most of all my gratitude goes

to my darling sister Ella, who has been my best friend, inspiration and support. Without you I would not have survived the most difficult times. Finally, and most importantly I would like to thank my love, Vincent for all the love and support you have given me. Your optimism and resilience are a great source of inspiration to me.

Espoo 7.1.2020

Hanna Viitala

Contents

1.	Introduction	9
1.1	Research Background	9
1.2	Objective of the thesis.....	10
1.3	New Scientific contribution	10
1.4	Thesis outline.....	10
2.	Heat recovery boiler of copper flash smelting process	11
3.	Corrosion theories	15
3.1	High temperature oxidation	15
3.2	Sulphur induced corrosion	17
3.2.1	Molten sulphates.....	17
3.2.2	Sulphuric acid induced corrosion	19
3.2.3	Corrosion by SO ₂	20
3.3	Chlorine induced hot corrosion.....	21
4.	Experimental methods	23
4.1	Thermogravimetry for measuring oxidation kinetics	23
4.2	Laboratory simulation of the heat recovery boiler	24
4.3	The quenching technique for phase diagram determination .	26
4.4	Scanning electron microscopy and electron dispersive spectrometry	30
5.	Thermodynamic modelling	31
5.1	Compound energy formalism	33
5.1.1	CuCl-ZnCl ₂ solid solution.....	35
5.1.2	FeCl ₃ -ZnCl ₂ solid solution	36
5.1.3	ZnCl ₂ -FeCl ₃ solid solution	37
5.2	Quasi-chemical model	37
6.	Results and discussion	40
6.1	Corrosion mechanism within the heat recovery boiler	40
6.2	Hot corrosion of carbon steel in the conditions of the heat recovery boiler	44

6.3	Corrosion resistance of AISI 304: The effect of Chromium alloying in the conditions of the heat recovery boiler	48
6.4	Corrosion resistance of AISI 316: The effect of Molybdenum alloying in the conditions of the heat recovery boiler	51
6.5	Corrosion resistance of Sanicro 28: The effect of nickel alloying in the conditions of the heat recovery boiler	53
6.6	Sulphuric acid induced corrosion.....	56
6.7	Microstructural considerations in corrosion prevention	57
7.	Conclusions	62
	References	64

List of Abbreviations and Symbols

ABBREVIATIONS

CALPHAD	Calculation of phase diagrams
EDS	Electron dispersive spectrometry
M	Metal
SEM	Scanning electron microscopy
Va	Vacancy

SYMBOLS

A,B,C,D	Elements A, B, C, D
A	area
a	model parameter for excess enthalpy
b	model parameter for excess entropy
c	number of components
D	diffusion coefficient
e	electron
f	number of degrees of freedom
G_m	molar Gibbs energy
G°	Gibbs energy of formation of a pure component
ΔG	Gibbs energy change
Δg	Non configurational Gibbs energy for cation-cation pair formation
ΔH	Enthalpy change
k	rate constant
k	Boltzmann's constant
L	Interaction parameter

Δm	weight change
N	Number of moles, number of atomic/lattice sites
N_A	Avogadro's constant
n	number of cation pairs
n	Index for oxidation rate law
P	Partial pressure (standard state 1 atm)
p	number of phases
Q	activation energy
R	The gas constant
ΔS	Entropy change
T	Temperature
t	Time
x	mole fraction
y	site fraction
Z	Coordination number
W	Number of different configurations of species
ζ	Ratio between first nearest and second nearest neighbours

SUBSCRIPTS AND SUPERSSCRIPTS

A, B, C, D	Components A,B,C,D
a, b	Components a and b
FNN	First nearest neighbours
i, j	Components i and j
m, n	stoichiometric numbers
mix	mixing
s_1, s_2	Sublattice 1 and 2
SNN	Second nearest neighbours

List of Publications

This doctoral dissertation consists of a summary and of the following publications, which are referred to in the text by their numerals. Articles are appended to this compendium in the same sequence.

1. Viitala, Hanna; Galfi, Istvan; Taskinen, Pekka, Initial oxidation behaviour of niobium stabilized TP347H austenitic stainless steel – Effect of grain size and temperature, *Materials and Corrosion*, 66 (2015) 851-862. DOI: 10.1002/maco.201407948.

2. Viitala, Hanna; Taskinen, Pekka, Hot Corrosion Mechanism of Steels Exposed to Heavy Metal Chlorides and Sulphates in SO₂ Environment, *Oxidation of Metals*, 86 (2016) 239-262. DOI: 10.1007/s11085-016-9634-z.

3. Viitala, Hanna; Taskinen, Pekka, Influence of nickel alloying on hot corrosion of stainless steels in SO₂-environment, *Materials Science and Technology*, 33 (2017) 49-64. DOI:10.1080/02670836.2016.1159371.

4. Viitala, Hanna; Taskinen, Pekka; Lindberg, Daniel, Experimental determination and thermodynamic optimization of the CuCl-ZnCl₂, ZnCl₂-FeCl₃, CuCl-FeCl₃, CuCl-CuCl₂, FeCl₂-FeCl₃, FeCl₂-CuCl₂ and CuCl-PbCl₂ phase equilibria, *Calphad Computer Coupling of phase Diagrams and Thermochemistry*, 67, 2019. DOI: 10.1016/j.calphad.2019.101667

Author's Contribution

Publication 1: Initial oxidation behaviour of niobium stabilized TP347H austenitic stainless steel – Effect of grain size and temperature.

The author designed and conducted the oxidation experiments and SEM-EDS analysis of the sample materials and wrote the first version of the manuscript under supervision and guidance of Professor Pekka Taskinen. Lic. Tech Istvan Galfi contributed to the sample preparation process by coating the samples with nickel.

Publication 2: Hot Corrosion Mechanism of Steels Exposed to Heavy Metal Chlorides and Sulphates in SO₂ Environment.

The author designed and constructed the experimental set up, conducted the corrosion experiments and SEM-EDS analysis of the sample materials and wrote the first version of the manuscript under supervision and guidance of Professor Pekka Taskinen.

Publication 3: Influence of nickel alloying on hot corrosion of stainless steels in SO₂-environment.

The author designed and constructed the experimental set up, conducted the corrosion experiments and SEM-EDS analysis of the sample materials and wrote the first version of the manuscript under supervision and guidance of Professor Pekka Taskinen.

Publication 4: Experimental determination and thermodynamic optimization of the CuCl-ZnCl₂, ZnCl₂-FeCl₃, CuCl-FeCl₃, CuCl-CuCl₂, FeCl₂-FeCl₃, FeCl₂-CuCl₂ and CuCl-PbCl₂ phase equilibria.

The author designed and constructed the experimental set up, conducted the equilibration-quenching experiments under supervision and guidance of Professor Pekka Taskinen, analysed the samples with SEM-EDS and carried out the thermodynamic modelling of the studied phase equilibria with assistance and guidance of Professor Daniel Lindberg. The author wrote the first version of the manuscript under guidance and supervision of professors Pekka Taskinen and Daniel Lindberg.

1. Introduction

1.1 Research Background

Smelting of sulphidic ores during the copper flash smelting process produces large quantities of SO₂-rich off-gas containing flue dust, which requires treatment due to its content of valuable metals, as well as due to its environmentally harmful properties. In the copper flash smelting process the flue dust containing gas is directed to a gas train, which purpose is to separate the dust from the process off-gas. The first step of the gas cleaning process is to separate most of the dust from the gas in a heat recovery boiler, which is also designed to recover the process heat for energy saving.

The process heat is recovered by radiation and convection to steel tube walls of the boiler, in which pressurized water circulates and absorbs the process heat, which is recovered as steam. The chemical environment inside the heat recovery boiler is likely too demanding for the use of typical carbon steel tubes, and more expensive clad-structured Cr-Ni alloyed steel tubes may be required. Material choices should not be made purely based on their price, because the possible damage and maintenance of the boiler may become more expensive in the long term than expected if the corrosion mechanisms are not well understood.

Finding optimal alloy composition for the steels used in the heat recovery boiler is challenging due to the chemically complex environment. It is also challenging to determine the optimal operation conditions for reducing the extent of corrosion of the heat recovery boiler. Some of the oxides, sulphates and chlorides of various heavy metals such as copper, iron, zinc, lead and arsenic composing the flue dust may together have low enough melting points to produce molten dust deposits inside boiler surfaces in the temperature range of the boiler walls (250 °C – 350 °C). Hot SO₂-gas may also react with moisture and oxygen to form sulphuric acid that may condense on the steel surfaces of the boiler at the operating temperature range of the boiler walls. Although, SO₂ exists in other typical boilers in energy technology, e.g. waste burning boilers, the process off-gas of the heat recovery boiler contains unusually high SO₂ concentrations and chemically complex flue dust. In this respect, understanding of the chemical environment exposing the heat recovery boiler to corrosion damage and the corrosion mechanisms helps to improve the efficiency of the copper production.

1.2 Objective of the thesis

Various heavy metal compounds and aggressive gas environment inside the heat recovery boiler cause corrosion, but the mechanism of it has been unclear due the synergistic effects of the complex chemical environment. Understanding the corrosion phenomena enables improved engineering and selection of corrosion resistant steels in terms of the steel's microstructure and chemistry. It is also important to investigate the phase equilibria and thermodynamics of the most central compounds found from the dust deposits, since little information concerning the melting behaviour of those compounds exists in literature. The research questions of this thesis are therefore:

- What are the hot corrosion mechanisms of the heat recovery boiler?
- Is molten salt corrosion possible in the environment of the heat recovery boiler?
- What is the influence of alloying elements on corrosion resistance of boiler steels in the chemical environment inside the heat recovery boiler?
- How to engineer an optimal corrosion resistant steel for the heat recovery boiler in terms of its microstructure?

1.3 New Scientific contribution

Hot corrosion induced by alkali salts for example NaCl, KCl, Na₂SO₄, K₂SO₄, as well as PbCl₂ and ZnCl₂ have been studied in different boiler applications such as waste burning, power plants etc. The corrosion environment of the heat recovery boiler contains oxides and sulphate and chloride salts of mainly Cu, Fe, Zn, Pb and As composing the flue dust. The synergistic effects of the complex dust in an especially aggressive gas atmosphere has not been studied much. The research has produced new information regarding hot corrosion caused by these compounds in an environment containing unusually high SO₂ concentrations and some new information regarding thermodynamics of some of the chlorides likely to exist in the copper smelter flue dust.

1.4 Thesis outline

This thesis is composed of four peer-reviewed journal articles, which are appended to this compendium (publications I - IV). Chapters 2 and 3 provide background information to this research in more detail. Chapter 2 describes the chemical conditions of the heat recovery boiler and Chapter 3 provides a short literature review of the corrosive properties of the various chemical compounds in the boiler. Chapters 4 and 5 describe the research methodologies used in this thesis. The experimental procedures are described in Chapter 4 and thermodynamic modelling in Chapter 5. The results and their discussion are presented in chapter 6 and finally, the conclusions are given in Chapter 7.

2. Heat recovery boiler of copper flash smelting process

The copper flash smelting process accounts for the world's largest production technology of primary sulphide-based copper [1]. Sulphidic minerals and oxygen react in the process to produce molten matte and slag releasing SO_2 , when dried chalcopyrite (CuFeS_2) concentrate, silica flux and recycle materials (flue dust) are ignited with oxygen of the blast in a hearth furnace. This results in controlled oxidation of the concentrates iron and sulphur, large evolution of heat and melting of the solids as the temperature of the furnace reaches around 1300°C . Most of the energy for heating and melting is derived from oxidation of iron and sulphur and the process is continuous and nearly autothermal. Copper is recovered as molten droplets of copper rich matte that settles at the bottom of the flash smelting furnace. 1 - 2 % of copper ends up in molten iron-silicate slag and as a result of copper vaporization during smelting the flue dust contains around 25 % of copper and other impurities from the ore. [1-3]

Between 3 and 10% of the feed material does not settle at the bottom of the furnace and is entrained in the process off-gas. This hot dust-laden SO_2 -containing (30 to 70 volume% SO_2) off-gas formed during smelting cannot be released into the atmosphere and it is therefore transferred into a gas cleaning process before it is used in the manufacture of sulphuric acid. The gas leaves the flash furnace at about 1400°C - 1300°C and the first step in the smelter off-gas treatment is cooling the gas for electrostatic precipitation of its dust. Gas cooling is done in a heat recovery boiler where the process heat is transferred by radiation and convection to the steel surface of the boiler's tube walls, in which pressurized water is circulated through 4 cm diameter tubes in the roofs and walls of the boiler and baffles on tube banks suspended in the path of the gas. The process heat is recovered as steam. [1-3]

The boiler consists of a radiation section (e.g. 25 m long x 15 m high x 5m wide rectangular chamber) and convection section (e.g. 20 m long x 10 m high x 3m wide). The size of the heat recovery boiler is designed to reduce the process off-gas temperature from around 1300°C as it enters the radiation section from the furnace to around 350°C at the exit of the convection section. [1, 2]

About 70% of the flash furnace dust is recovered in the cooling system when it falls out of the waste heat boiler gases due to its low velocity in the large boiler chambers. The dust is collected and usually recycled to the smelting furnace for improved copper recovery. It is occasionally treated hydrometallurgically, which avoids recycling impurities back to the smelting furnace and allows the furnace to smelt more concentrate. The remaining 30 % of the process dust is caught in the electrostatic precipitators before the SO_2 -rich process off-gas enters the sulphuric acid plant. [1] Figure 1 shows the structure of the flash furnace and the heat recovery boiler [4].

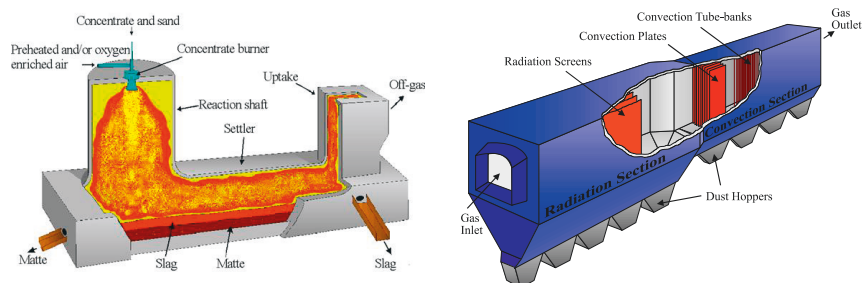


Figure 1. Structure of the flash smelting furnace and the heat recovery boiler [4].

The dust particles that enter the boiler with the gas consist mainly of metallic oxides, such as Cu_2O and Fe_3O_4 . In the radiation part, the temperature of the dust and off-gas mixture cools down to $700\text{--}500^\circ\text{C}$ and oxide dust particles begin to react with SO_2 , forming sulphates. These reactions are highly exothermic causing an increase in particle temperatures softening them. Sulphate bridges found between the flue dust particles in the accretions suggest that the sulphate phase is the binding component that results in the formation of dust accretions on the heat recovery boiler walls. When sulphated particles are close to their sintering temperature, they may stick to the heat transfer surfaces of the boiler. For this reason, it is desirable that the sulphation reactions take place in the radiation section of the boiler, before the dust particles come in contact with the boiler walls. [3]

Generally, two types of dusts are present in the copper flash smelter off-gas. Mechanically formed dust forms as a result of the entrainment of small solid and/or liquid particles from the concentrate into the process off-gas. Chemical dust formation is caused by the vaporisation of components in the concentrate, followed by their condensation as dust particles at lower temperatures in the heat recovery boiler. [2]

Mechanically formed flue dust consists mainly of copper and iron oxide particles, which are surrounded by sulphate surface. This type of dust has a coarser particle size. Elements having low melting temperatures and their oxides and sulphides, often have high vapour pressures and tend to vaporise during flash smelting, forming chemical dust. Chemical dust has a very fine particle size because of the nucleation and growth processes occurring as the process off-gas cools down. An example of the structure and differences of copper smelter flue dust particles is shown in Figure 2. These small particles may also condense on the surface of larger, mechanically entrained particles. In copper smelting processes, easily volatile components include Ag, As, Pb, Sb, and Zn. Copper also vaporises in the hot combustion zone of the furnace. Oxygen enrichment increases the combustion temperature in the flash furnace reaction shaft and, as a result, more copper is vaporised. The vaporised copper particles are very fine and easily drift out of the furnace with the off-gas. [2]

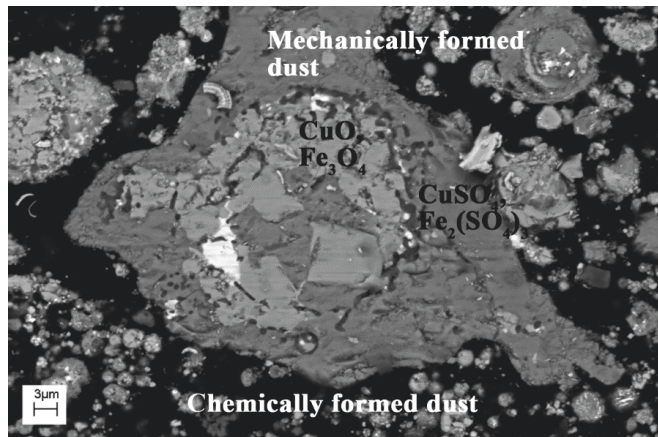


Figure 2. A scanning electron microscope image of a cross section of copper smelter flue dust sample. The mechanically formed dust is composed of the large particles, while the chemically formed dust is composed of the small particles.

The dust build-ups on the boiler walls are formed partly by a direct impact of particles and partly by vapour condensation. According to Miettinen et al. [2] the initial deposition takes place by the condensation of vapours that contain zinc, lead, arsenic and other substances having high vapour pressures. Also, low melting point eutectics of alkali salts such as chlorides and sulphates can act as sticky cohesive particles attaching to the boiler walls. The fine particles landing on the surface of the porous dust deposit react in the SO_2 -rich atmosphere at boiler wall temperatures to sulphates. The process gas within the boiler contains SO_2 , O_2 , SO_3 , H_2O , H_2SO_4 and N_2 that diffuse into the porous accretions to form a stagnant gas layer within the dust deposit. The composition of this gas layer may differ greatly from the composition of the process gas flow on the surface of the accretion layer. Locally HCl and H_2SO_4 may form within the dust deposit, and even reducing atmosphere may exist locally, allowing new reactions of acid (wet) corrosion to take place. The atmosphere within the deposit may enable metal sulphates to be reduced to secondary sulphides and even metallic components. Within the dust accretion layer, compounds may form that would not be stable in the bulk atmosphere of the boiler. [2] This may be a possible mechanism by which chlorides of Cu, Fe, Pb and Zn form within the deposit. These dust deposits can cause severe operational problems, such as reduced heat transfer efficiency and corrosion.

The heat recovery boiler of the copper flash smelter is a demanding corrosion environment. In addition to the complex chemistry of the dust deposits containing heavy metals in the form of sulphates, oxides and chlorides, sulphur may also cause low-temperature corrosion. When SO_3 and H_2O coexist in the boiler atmosphere, they react to form sulphuric acid (H_2SO_4) according to reactions (1) – (2). Below the acid dew point temperature, gaseous sulphuric acid condenses as small corrosive drops on boiler walls. The rate of sulphuric acid condensation in addition to temperature is also dependent on H_2SO_4 concentration of the gas. The higher the H_2SO_4 concentration in the gas, more readily it condenses as liquid. The liquid H_2SO_4 and H_2O mixture forms an azeotrope, meaning that the composition of the condensate contains more than 70

mol% of H_2SO_4 . [5] The dew point of H_2SO_4 determines the lowest safe metal temperature because liquid sulphuric acid causes acidic dissolution of the steel's protective oxide scale. [6-8]



Below 500 °C, oxidation of SO_2 to SO_3 is a thermodynamically favored reaction. However, SO_3 formation has slow reaction kinetics and only a small portion of SO_2 is eventually oxidized to SO_3 . 1 - 3% of sulphur dioxide is estimated to react to SO_3 within the heat recovery boiler atmosphere, depending on the rate of gas cooling. Slow cooling produces a higher amount of SO_3 , since long residence time is needed to achieve the maximum SO_3 concentrations [3, 9]. The rate of SO_3 formation is dependent on SO_2 and O_2 partial pressures in the gas, temperature and the amount of catalysts available. For example, oxides such as Fe_2O_3 , CuO etc. in the copper smelter flue dust have strong catalytic effect on SO_2 oxidation. According to Sarkar et al. [9], the oxidation rate of SO_2 to SO_3 is highest at the temperature range of 570 °C – 640 °C and according to Ranki-Kilpinen et al. [3] at 760 °C, after which the reaction becomes slower again. Oxygen is fed to the gas for the purpose of enabling the oxide dust particles to form sulphates with the SO_2 . The amount of air must be correct, because too small concentration leads to incomplete sulphation of oxide particles. However, excess of O_2 and H_2O in the gas leads to an increase in the SO_3 concentration of the gas. H_2O in the gas increases the SO_2 oxidation rate via oxidation of the HOSO_2 species. The sulphation of the dust particles and oxidation of SO_2 are competing reactions and an oxygen concentration that exceeds the necessary concentration for sulphate formation from the oxides in the dust, leads to an increase in the SO_3 concentration of the gas. Due to the complexity of the flue dust, an accurate prediction of SO_3 concentration in the heat recovery boiler gas is difficult. [3, 5, 9, 10]

The sulphuric acid dew point temperature is very sensitive to the SO_3 concentration in the gas and increase of SO_3 concentration leads to increase in acid dew point temperature at a given H_2O concentration. [7] The amount of SO_3 in the heat recovery boiler gas atmosphere can be adjusted by controlling the above-mentioned parameters. However, inside the porous dust accretion layer, SO_3 concentration may differ from the gas atmosphere of the boiler, due to reactions within the dust deposit.

In the next chapter, the corrosion mechanisms caused by the chemical components present in the heat recovery boiler are discussed.

3. Corrosion theories

3.1 High temperature oxidation

In the beginning of an oxidation process, oxygen reacts with the most reactive element in the alloy and forms the most stable oxide. [11] The type of oxide formed on the steel surface depends on the Gibbs energies of the oxidation reactions. The most stable oxide formed is the one with the most negative Gibbs energy, requiring the smallest oxygen partial pressure. [12, 13] Figure 3 shows that chromium oxide requires the lowest oxygen partial pressure to form compared to the other major alloying elements in the boiler steel (Fe and Ni) and thus Cr_2O_3 is formed before other oxides of the steels alloying elements, in a few minutes of exposure to oxidizing atmosphere. [11]

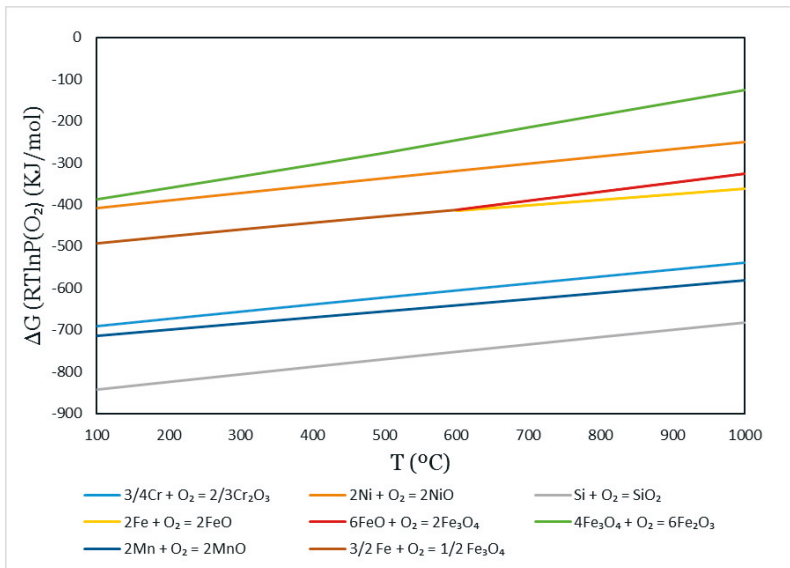


Figure 3. Gibbs energies of the oxide formation reactions of the steel's alloying metals calculated by HSC version 8.1 with MainDB8 database.

Oxide growth rate is influenced by the dissociation rate of an oxidizing molecule such as H_2O or O_2 on the steel or oxide surface and by the diffusion properties of cations and anions through the oxide scale. Dissociation rate of the oxidizing molecules is dependent on the catalytic activity of the steel or oxide surface, which is affected by structure of lattice defects and alloying elements of the steel. Cationic sites in the oxide lattice react with electron donors such as O_2 and H_2O and oxygen sites react with electron

receiving ions. In general, stoichiometric oxide surfaces are less reactive, because gas absorption becomes easier due to surface defects and uneven oxide surfaces. [14]

Oxide scales are semiconductors, in which the transport of metal ions takes place through lattice defects towards the oxide/gas interface, where they react with oxygen, forming oxide. Electrons are transported through electron holes towards the oxide surface where they react with absorbed oxygen molecules, which then react to form oxygen anions (O^{2-}). As electrons move from the steel surface through the oxide to the oxide/gas interface, cation vacancies and electron holes move from the oxide/gas interface towards the oxide/steel interface where they coalesce together, forming pores. [15] Metal and oxygen ions move in opposite directions through the oxide scale and the oxide thickens inwards and outwards from the original oxidation surface [16, 17].

Optimal corrosion resistance is achieved when the formation of a protective scale has low porosity, good adherence, high mechanical and thermodynamic stability and slow growth rate. [12] Oxides containing high number of lattice defects result in fast oxidation rates of steel. Cr_2O_3 , Al_2O_3 and SiO_2 contain the least amount of lattice defects and are thus the most protective types of oxides providing best insulation for the steel from the surrounding atmosphere. [13] SiO_2 is an excellent diffusion barrier, which in addition to low amount of lattice defects is also attributed to the absence of grain boundaries in vitreous silica. SiO_2 also forms intrusions along the alloy grain boundaries and improves oxide adhesion by mechanical keying. [18-20]

During oxidation the steel surface beneath the oxide becomes depleted of chromium and iron starts to diffuse into the chromium oxide transforming it into a $FeCr_2O_4$ spinel structure. The spinel contains more lattice defects than stoichiometric Cr_2O_3 and diffusion of the other alloying elements such as manganese, iron and nickel through the oxide becomes easier. Also, oxygen diffusion from the oxide towards the steel surface becomes faster and the oxidation rate increases. [13, 21] The alloying elements of steel diffuse in the chromium oxide along Cr^{3+} lattice sites. Manganese diffuses fastest in the oxide and dissolves in it when the steel surface beneath the oxide is depleted of chromium, which is why it is found on the top layers of the oxide scale. Eventually $MnCr_2O_4$ spinel is developed on top of the chromium oxide with manganese alloyed steels. Iron and nickel have approximately the same lattice diffusion rates, but from these two elements nickel diffuses slower along the grain boundaries. The diffusion coefficients of steel's alloying elements in Cr_2O_3 become smaller in the following order: $D_{Mn} > D_{Fe} > D_{Ni} > D_{Cr}$. [22]

Oxidation resistant steels must contain large enough percentage of chromium (>18 wt%) so that the chromium flux towards the steel surface is large enough to provide material for chromium oxide formation on the steel surface, since chromium diffusion in the steel matrix towards the oxygen potential is faster than oxygen diffusion into the steel matrix. However, this concentration depends on the diffusion properties of chromium in the steel. [11] As oxygen anion diffuses through the oxide scale, the chromium concentration at the steel surface needs to be large enough so that the uniform Cr_2O_3 scale can be maintained. [23] To prevent oxidation damage, it is necessary to make the supply of chromium from the steel to the oxide/steel interface high enough to compensate for the chromium consumption by oxidation. Adding more chromium is a normal solution to improve the steel's oxidation resistance. However, increasing the chromium

content is always accompanied with increased precipitation of embrittling Cr-rich phases and a reduction of creep resistance. [24]

For ferritic and austenitic high-alloyed steels used in high temperature environments, the formation of a dense, well adherent, slow-growing Cr_2O_3 layer provides optimum protection against oxidation and sulphation by gas atmospheres and against attack by corrosive deposits. It is most advantageous if such a layer is formed in the very first operation run of a plant or even better if it is generated by a controlled pre-oxidation done at a low oxygen partial pressure, for example in a wet $\text{N}_2\text{-H}_2$ atmosphere so that iron or nickel oxides are not formed. Steels covered by a dense Cr_2O_3 layer are most resistant to every type of corrosion. However, if the layer does not grow rapidly enough, there will be considerable absorption of corrosive elements into the alloy, which affects negatively the oxide formation. [25]

Ions diffuse in the steel and through oxide scales by different mechanisms in addition to vacancy diffusion. Dislocations, pores, surfaces and grain boundaries provide fast diffusion routes for steels alloying elements compared to diffusion via lattice vacancies. [20] In the initial oxidation stage, Cr_2O_3 formation is promoted by the fast outer flux of chromium along the steel grain boundaries which serve as a “short-circuit” for chromium supply to the oxidation front. This protective oxide layer begins to spread from the grain boundaries towards the grain surfaces. Short lateral diffusion distances on the fine-grain steel allow a rapid spreading of protective external Cr_2O_3 scale over the entire steel surface. If Cr_2O_3 oxide layer does not densely cover the entire surface, the intra-grain regions of the oxide scale far enough from the grain boundary are dependent on chromium supply by lattice diffusion. These areas cannot maintain sufficiently high chromium concentration and the oxide begins to convert to the iron-rich oxides by the outward iron diffusion leading to the formation of Fe_2O_3 nodules top of the oxide and inward oxygen transport results in formation of FeCr_2O_4 spinel. Thus, grain refinement is another approach to improve oxidation resistance without additional elements or increasing the chromium content of the steel. [18, 24-28]

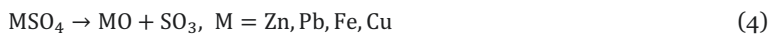
3.2 Sulphur induced corrosion

3.2.1 Molten sulphates

Hot corrosion by molten sulphates is a dissolution and reprecipitation process, in which acid/base nature of a sulphate salt causes dissolution of steels protective oxide scale. [17, 29] Oxide ions in sulphate melts are formed by dissociation of the sulphate ion according to reaction (3).



Molten sulphates dissociate on the steel's surface oxides according to reaction (4).



The basicity of the melt is a function of the O^{2-} or MO activity. The higher the MO activity, the more basic the melt becomes. At low MO activities, the sulphate melt is more acidic. Activity of the MO species depends on the SO_3 partial pressure of the gas.

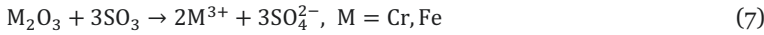
Generally, in an atmosphere containing a low concentration of SO_3 , molten salt is more basic, whereas in an atmosphere containing high concentration of SO_3 acidic conditions are established. [30]

Besides the effect of gas composition, the basicity of a molten sulphate also depends on the melt components. Sulphate melts containing ZnSO_4 , PbSO_4 or other heavy metal sulphates are more basic than alkali sulphate melts. The solubility of steel's oxide scales in molten sulphates is the most important factor of corrosion rate. [30]

Oxides that dissolve in sulphate melts break down as well to basic and acidic solutes and their concentrations in the molten sulphate layer depend on the melt basicity [29]. Oxide scale dissolution under molten sulphates happens either by basic or acidic fluxing. Basic fluxing takes place when the steel's oxide reacts with O^{2-} ions in basic melts producing soluble basic oxide species according to reactions (5) and (6). [30]



Acidic fluxing occurs in acidic melts when the steel's oxide reacts with dissolved SO_3 according to reactions (7) and (8). [30] Acidic solutes create a positive solubility gradient resulting in slower corrosion rates, whereas negative solubility gradient resulting in rapid corrosion rates is created by the formation of basic corrosion products. [29]

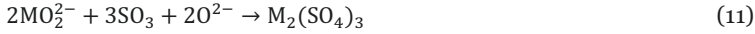


The important oxides of steel all have low solubilities in sulphate melts. However, the hot corrosion reactions often proceed very rapidly. This is a result of continuous mass transport within the melt when an activity gradient is established. The driving force of basic fluxing of the steel's oxide film is maintained by the creation of an MO/O^{2-} gradient in the molten sulphate film. Oxide ion activity increases towards the melt/oxide boundary by the oxidation of metal and the formation of sulphide MS according to reactions (9) and (10).

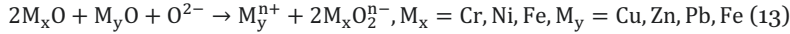
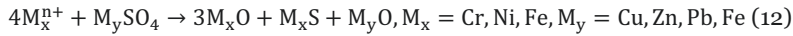


MO/O^{2-} activity gradient exists if the solubility decreases monotonically with increasing distance into the sulphate layer. Thus, the thickness of the melt film in combination with the gas phase composition are of significance to the hot corrosion rate. The chemistry of thick salt films is mainly determined by the reactions taking place at the oxide melt interface, whereas the chemistry of thin salt films strongly depend on the composition of the gas atmosphere. [30] Precipitation increases when the distance from the steel/melt interface increases, leaving less metal in the melt and resulting in diffusion flux due to activity gradient. High SO_3 concentrations near the melt/gas interface stabilize basic fluxing into the molten sulphate by maintaining acidic conditions. This way, the activity gradient of the basic component is established. [17, 29]

The consumption of SO_2 and O_2 at the oxide/steel boundary results in increase of O^{2-} activity. The concentration of dissolved oxide scale species MO_2^{2-} is highest at the melt/oxide boundary and lowest at the melt/gas boundary. As a result, dissolved oxide species diffuse through the melt film towards the gas atmosphere where the O^{2-} concentration is lower and where they precipitate as sulphates, according to reaction (11). The scales formed by basic fluxing mechanism grow fast, are porous and non-protective. [30]



As molten salt penetrates the oxide scale at some locations, steel surface comes to contact with low oxygen partial pressure and high sulphur activity resulting in sulphide formation according to reaction (12). At the cathodic reduction site, the local basicity increases as a result of the formation of sulphides beneath the oxide, since MO is a reaction product. Sulphidation changes the salt chemistry because it produces basic corrosion products (MO_2^{2-}). Sulphur activity decreases as it is bound in the sulphide resulting in the increase in basicity of the melt according to reaction (13). [17, 29]



In the case of an oxide film consisting of two different oxides, the more basic oxide should release oxide ions as a corrosion product thus exhibiting acidic dissolution. Meanwhile the acidic oxide reacts with those oxide ions, which results in the basic dissolution of the more acidic oxide in the molten sulphate. The dissolution behaviour of the two oxides supports each other and consequently the fluxing of the oxide scale proceeds faster compared to the situation where the oxide scale is composed of only one oxide. The dissolution kinetics of acidic Cr_2O_3 becomes faster when combined with Fe_2O_3 and much higher kinetics is established in the presence of very basic oxides such as NiO . The acidic oxide providing the oxide ions causes the acidic solubility of an otherwise protective oxide to increase. [29]

3.2.2 Sulphuric acid induced corrosion

Condensation of liquid sulphuric acid film on the oxide surface below its dew point temperature causes acidic fluxing of the steel's oxide scales. Sulphuric acid dissociates on the oxide surface according to reaction (14). In acidic fluxing, dissolution of the steel's oxide takes place by the formation of M^{n+} -ions and SO_4^{2-} -ions, which produces unprotective sulphate scales according to reactions (15) and (16). [6]



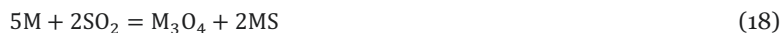
Water produced by the dissociation of sulphuric acid when coming in contact with the oxide scale, may lead in addition to formation of OH^- and H^+ ions when H_2O molecule dissociates on the oxide surface. H^+ can cause protonic defects in the oxide lattice, changing the microstructure of the scale and its diffusion properties. OH^- ion is much smaller compared to O_2 , which leads to a higher diffusion rate of oxygen through the oxide scale, increasing the oxidation rate. [14, 31]

3.2.3 Corrosion by SO_2

Metal sulphides are formed as corrosion products by molten sulphate induced corrosion by fluxing of the oxide, or by penetration of SO_2 gas through the scale, enabling it to react with the steel surface. SO_2 molecules can migrate through the scale via cracks and pores. As SO_2 reaches the steel surface, it dissociates to S_2 and O_2 according to reaction (17). Sulphur can diffuse into the steel along grain boundaries and the thermodynamically most stable metal sulphide will form when sulphur activity increases high enough. Sulphur activity reaches high values, because below the oxide scale, oxygen activity is small, as oxygen has been consumed in the oxide formation [32, 33]. The difference between sulphur and oxygen anion sizes leads to M-S bond lengths longer than the corresponding M-O distances. In ionic crystals, this leads to smaller lattice energies for the sulphides and in lower Gibbs energies for the sulphide formation. [17] Continuing sulphide precipitation removes steels alloying metals from the surface inhibiting protective oxide scale growth. [33, 34]



Formation of sulphide will reduce the sulphur activity at the steel surface to the value equal to the dissociation pressure of the sulphide in question. The formation of oxide and sulphide continues as long as the sulphide forming metal activity in the scale between gas and the steel surface is high enough to keep the equilibrium of the reaction (17) on the right side. If sulphur transport from the atmosphere continues, eventually the next most stable sulphide will start to precipitate. [33, 34] Oxidation of MS releases SO_2 , which can migrate further towards the steel/scale interface reacting again to MS according to reaction (18). [34]



The activity of the metal forming sulphide is dependent on the diffusivity of metal cations in the steel and through the scale. When the conditions of reaction (18) are no longer satisfied, only oxide is formed. A mixed oxide/sulphide scale is eventually overgrown by oxide. Oxidizing species in the SO_2 atmosphere (H_2O and O_2) promote oxide formation. Metal cation diffusion is slowed down by oxide scale and metal activity decreases towards the oxide surface. [34]

Most metal sulphides grow according to parabolic kinetics, controlled by solid state diffusion. However, the growth rates of most sulphides are much faster than the corresponding metal oxidation rates. Especially the transition metal sulphides of Fe, Cr and Ni display large deviations from stoichiometry having high point defect densities, predominantly cationic vacancies. The high defect densities of the simple metal sulphides result in high diffusion rates and rapid sulphide growth. [17]

Due to its higher negative value of Gibbs energy, chromium sulphide will precipitate before iron and nickel sulphides can form [34]. Increased sulphur activity below the scale and simultaneous chromium depletion of the steel surface by the formation of CrS or volatile chromium compounds may result in the formation of highly defective nickel sulphides, efficiently preventing the formation of a protective oxide scale. [35, 36]

The growth of a sulphide scale takes place as metal cation diffuses towards the oxide/sulphate interface while vacancies migrate simultaneously towards the oxide/steel interface. Vacancy injections eventually result in void formation. MS dissociates on the surfaces of these voids to produce sulphur vapour, which again reacts with the steel, forming an inner layer of MS. The continuing growth of the sulphide scale proceeds inwards from the steel surface. [36]

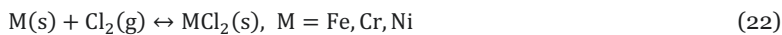
3.3 Chlorine induced hot corrosion

At elevated temperatures, chlorine compounds trigger a corrosion mechanism referred to as active oxidation, in which molecular chlorine released from these compounds acts as a catalyst for the uncontrolled oxidation of the steel. Oxidation of metal chlorides such as ZnCl_2 , CuCl_2 , FeCl_2 etc. to oxides and consequent release of molecular chlorine results in a self-sustaining cycle of chlorine induced corrosion. Chlorine is released according to reactions (19) - (21). [32, 35, 37 – 47]



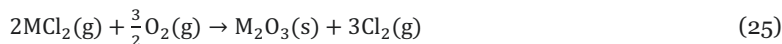
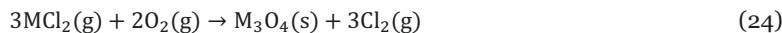
Chlorine is able to penetrate the protective oxide scale at the steel surface through pores and cracks and reach the scale/steel interface. The penetration of chlorine species through the oxide scale is still not fully understood. It seems that neither solid state diffusion, grain boundary diffusion, nor molecular diffusion through cracks and pores of the scale are fast enough to explain the high oxidation rates of steels. It is concluded, that somehow the chlorine itself must affect the creation of fast diffusion paths, possibly by creating grooves and fissures at the steel grain boundaries. [32, 35, 37 – 47]

At the scale/steel interface, oxygen is consumed by the formation of metal oxides resulting in conditions of high Cl_2 partial pressure and low O_2 partial pressure. In these circumstances, metal chlorides become stable. Chloride formation according to reaction (22) is a spontaneous reaction typically having a large negative Gibbs energy of formation. [32, 35, 37 – 47] Metal chlorides tend have high vapour pressures even at low temperatures resulting in vaporization (23) and rapid loss of metal from the steel surface.



Metal chlorides diffuse towards the scale/gas interface through the oxide scale. The oxygen partial pressure increases in the scale towards the scale/gas interface and at

areas of higher oxygen activities the metal chlorides precipitate as oxides according to reactions (24) – (25) contributing to further scale growth and thus accelerated corrosion. As a result, the oxide scales formed according to this mechanism are loose and highly porous enabling fast material transport away from the corroding steel. [32, 35, 37 – 47]



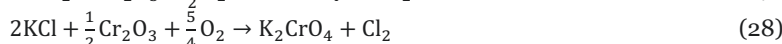
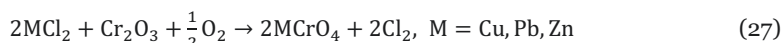
By reactions (24) – (25) free chlorine is again released and part of it diffuses to the gas phase and part of it diffuses to the steel surface. This way, a cycle is formed. The chlorine cycle provides a continuous transport of steel's alloying metals away from the metal surface toward higher oxygen partial pressures in the scale. The total consumption of chlorine is small, which is why it can be considered as a catalyst for the oxidation of steel. The net reaction is (26). [32, 35, 37 – 47]



The second important effect of chlorides causing significantly accelerated corrosion attack is their ability to lower the initial melting temperatures of the salt deposits in which they occur. Chlorides such as ZnCl_2 , PbCl_2 , CuCl , FeCl_3 etc. have been shown to lower the melting temperatures of the salt mixtures considerably [39 – 42, 48]. The lowering of the melting temperature of a salt mixture increases further when more heavy metal salt compounds such as chlorides or sulphates are present in the mixture. These deposits flux the steel's oxide scale [32, 38, 40]. The rate at which the sulphate and chloride ions dissociate on the steel's oxide surface determines the corrosion rate [36].

The detrimental effect of molten salt phase is based on the better contact between the salt particles and the steel surface. When a molten salt layer is formed above the oxide, the salt can easily wet the oxide surface and penetrate through the pores and cracks. Molten salt provides a medium for fast migration of oxidants inwards towards the steel surface and dissolved metal ions outwards towards the scale/gas interface. A liquid salt mixture provides an electrolyte, a pathway for ionic charge transfer, resulting in fast electrochemical corrosion attack. [32, 35, 38, 40, 45]

The third detrimental influence of chlorine containing species occurs via dissolution of the steel's protective oxide scale by the formation of chromates according to reactions (27) – (28). Chromate formation effectively prevents the formation of a continuous oxide scale. This type of oxide scale breakage opens a path for Cl_2 to cause chlorination of the steel surface since chromates are not protective corrosion products due to the depletion the oxide of chromium. Consequently, chromia can be replaced by less protective iron oxides. [29, 35, 38, 40-44, 48]



4. Experimental methods

4.1 Thermogravimetry for measuring oxidation kinetics

The effect of grain size on the oxidation behaviour of steel was studied by comparing the oxidation behaviour of the same austenitic stainless steel TP347H with two different grain sizes. The samples were cut from a commercial superheater tube material into approximately 6 mm x 6 mm x 60 mm bars. Chemical analyses of the steels are given in Table 1. Before the oxidation experiments, the samples were polished with SiC-papers P240, P400, P800 and P1200. After polishing, the samples were washed in ethanol in an ultrasonic bath for 10 minutes.

Table 1. Chemical compositions of the studied steels.

Weight%	Cr	Ni	Si	C	Mn	Nb	P	S	Ta	Fe	Grain size/ASTM
TP347H	17.34	11.07	0.56	0.053	1.58	0.73	0.024	0.0007	0.005	bal.	5.5
TP347HFG	18.3	11.5	0.43	0.09	1.5	0.88	0.024	0	0.002	bal.	9.1

The oxidation was carried out at 600 °C, 650 °C, 700 °C and 750 °C by placing the steels in a Lenton UAF 16/10 chamber furnace (Hope Valley, UK) where they were hung above a calibrated S-type thermocouple. The steels were weighed twice a day in the beginning of the experiment and once a day for the rest of each experiment with a calibrated Mettler Toledo AB204-S semi-microbalance (measurement accuracy ± 0.1 mg). The steels were weighed three times in order to get an average mass at each measurement point. The weight change of the steels was measured with this method, because the oxidation rate of the steels was small, requiring the best possible recording accuracy. The duration of the gravimetric experiments was more than 200 hours at each experimental temperature and each run was repeated three times. Also an experiment was done, during which the steels were left in the furnace at 650 °C without removing them for the weight change measurements in order to check whether temperature cycling has an effect on the oxidation behaviour. The extent of temperature cycling was so small that it had no effect on the obtained mass gains or the structure of the oxide scales formed. Air dried with silica gel was led to the chamber furnace at the rate of 320 mL/min in order to eliminate the effect of moisture and the external atmosphere.

The obtained oxidation rates were calculated with the rate equation (29)

$$\left(\frac{\Delta m}{A}\right)^n = kt, \quad (29)$$

where n is an index characteristic to the oxidation mechanism of the steel, k is the rate constant, $\Delta m/A$ is the observed weight change per unit area and t is oxidation time [49]. Activation energy of the oxide scale formation Q can be calculated from linearization of the Arrhenius equation (30) according to (31)

$$k = Ae^{-Q/RT}, \quad (30)$$

$$-\ln k = -\ln A + \frac{Q}{RT}, \quad (31)$$

where R is the gas constant, T is temperature in Kelvins and A is a constant. [49] The results of these measurements and calculations are presented in more detail in Article 1.

4.2 Laboratory simulation of the heat recovery boiler

In order to investigate the corrosion phenomena occurring in the heat recovery boiler of the copper flash smelting process, typically used steels, one low alloy steel and three high alloy steels were chosen as test materials. The heat recovery boiler's walls are made of carbon steel tubes coated by more corrosion resistant stainless steel. The chemical compositions of the used steels are shown in Table 2.

Table 2. Chemical compositions of the steels used in heat recovery boiler.

Steel/wt%	C	Si	Mn	P	S	Cr	Mo	Ni	Cu	Al	Ti	Fe
P235GH	0.09	0.21	0.47	0.005	0.005	0.09	0.02	0.08	0.15	0.022	0.027	98.83
AISI304	≤0.08	0.54	1.81	≤0.045	≤0.030	18.21	0	9.66				67.24
Sanicro 28	≤0.03	0.54	1.80	≤0.03		25.45	4.37	30.05	0.53			33.89
AISI316	≤0.08	0.55	1.61	≤0.045	≤0.030	17.4	3.12	10.37				67.14

The steels were exposed to an atmosphere that simulates the conditions of the heat recovery boiler. The steel samples were placed in a horizontal tube furnace (Lenton CSC 12/--600H, controller by Eurotherm) that has a quartz glass work tube, in which a gas mixture of composition 43 vol% SO_2 , 39 vol% N_2 , 9 vol% O_2 and 9 vol % H_2O was led. The air was dried beforehand with silica gel. Water was introduced to the furnace space using a peristaltic pump (ISM596 Reglo digital; Ismatec Oak Harbor, Washington) by which tap water was pumped through a long alumina capillary in the hot section. This way, small amount of water could be dosed accurately into the furnace, since the water flow is dependent on the capillary tube diameter used in the pump.

Temperature of the furnace hot section was measured by calibrated PT100 resistance sensors that have a measurement accuracy of ± 0.1 °C. The resistance sensors were connected to Keithley 2010 DMM multimeters. The temperature was measured from the middle and from the edge of the sample holder. The maximum temperature difference between the samples was 8 °C at 250 °C, 6 °C at 300 °C and 4 °C at 350 °C.

Isothermal corrosion experiments were done at 250 °C, 300 °C and 350 °C to simulate the temperature variations taking place on the heat recovery boiler walls. The steels were covered by deposit containing 65 wt% of copper smelter flue dust, 5 wt% potassium chloride (KCl) and 30 wt% of zinc chloride ($ZnCl_2$). In the reference condition, the steels were covered by a deposit containing 95 wt% copper smelter flue dust

and 5 wt% of KCl. The total amount of dust and chloride deposition on the steel samples was approximately 0.3 g/cm². In the flash smelting furnace at 1300 °C, chlorine in the ore vaporises and is found in varying amounts in the copper smelter flue dust. When chlorides gather in the deposits over the years they result in fast corrosion. ZnCl₂ was added to the copper flash smelter dust to study its effect and to accelerate the corrosion rate to simulate years of boiler operation. A small amount of KCl is also typically present in the dust [2].

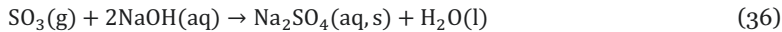
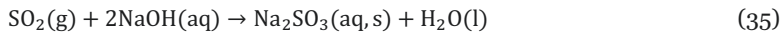
The deposits were mixed carefully and put on the grinded and cleaned boiler steels, cut in 10 mm x 10 mm sized pieces, and annealed in the furnace for two weeks. The mixtures were not homogenized by melting before the corrosion experiments. Particle sizes of the deposit components were measured by laser diffraction (Malvern Instruments, UK). Chemically formed dust in the copper smelter flue dust had an average particle size of 2,4 µm and the mechanically formed dust had an average particle size of 239 µm. Average particle sizes of ZnCl₂ and KCl were 825 µm and 220 µm, respectively. The chemical composition of the copper smelter flue dust is shown in Table 3.

Table 3. Chemical compositions of the copper smelter flue dust. The flue dust was analysed by ICP (Inductively coupled plasma spectrometry) and XRD (X-ray diffraction).

Copper smelter flue dust	As	Bi	Cd	Cu	Fe	Ni	CaO	MgO	Pb	Zn	Al ₂ O ₃	K ₂ O	SiO ₂	S
Oxygen is not analysed	3.1	0.62	0.95	18.4	17.2	0.1	1.33	0.44	3.6	5.2	0.9	0.69	3.8	10.3
Phases identified by XRD	Fe ₃ O ₄ , CuSO ₄ , Cu _{0.5} Zn _{0.5} Fe ₂ O ₄ , Cu ²⁺ 2(AsO ₄)(OH), FeAsS, Cu ₂ AsO ₄ (OH) ₃ , Fe ₂ (SO ₄) ₃ , PbSO ₄ ·PbO, CuFe ₂ S ₃ , Fe _{1-x} S, ZnSO ₄													

Prior to the corrosion experiments, the steel samples were polished with SiC-papers P240, P400, P800 and P1200 and washed in ethanol in an ultrasonic bath for 10 minutes. After the corrosion test, the steel specimens were cooled to room temperature in a nitrogen atmosphere.

The SO₂ and SO₃ gases from the furnace outlet were led to a gas washing system. The gas flowed through hydrogen peroxide (33 %) and sodium hydroxide (13 mol/l) solutions, because under pressure was created in the gas train by an under pressure pump (Lab vac H40, Piab Sweden). The gas was cleaned by washing reactions (32) - (36).



The hydrogen peroxide is stabilized by acid formation, but on the other hand, its dissociation to water and oxygen becomes faster as temperature increases due to the exothermic reaction (34), and due to the exposure to light. Because of these uncertainties in the estimation of the consumption of hydrogen peroxide, NaOH solution was used as a backup for the gas cleaning. To be sure that SO_x gases cannot get past the gas washing system after exiting the furnace, the exhaust gas was led through a strong so-

dium hydroxide solution. The solution was dyed blue using bromotymol blue as an indicator. Bromotymol blue changes its colour to green at pH 6.0 – 7.6, indicating when the sodium hydroxide in the solution has been consumed. The danger in this method is that the pipes in the gas washing bottles get easily blocked due to the formation of sulphate crystals. During the maintenance of the first gas washing line, a similar parallel gas washing train was used, and the gas flow was guided through it using valves. A schematic flow diagram of the experimental set up is presented in Figure 4.

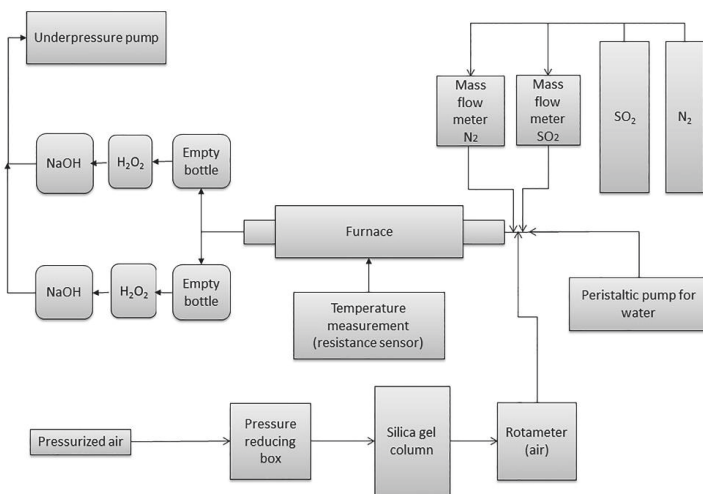


Figure 4. Flow chart representing the experimental set up used in the hot corrosion experiments.

After the corrosion experiment, a chlorine free resin (Glass clear polyester resin by Eli chem resins, UK) was used to cover the dust embedded samples. This resin was chosen, because epoxy was found to react with chlorides in the deposit. After the resin had cured, extra resin was cut off and the samples were cast in epoxy in order to prepare metallographic cross sections for the SEM-EDS analysis. The cross sections were polished with SiC-papers P80, P240, P400, P800, P1200, P2000 and P4000. The polishing process was water-free in order to avoid dissolution of chlorides and a mineral oil (Shell Ondina) was used as a lubricant. The oil was removed by washing the samples in petroleum ether in an ultrasonic bath after which the cross sections were coated with carbon for better conductivity during electron microscopy. Due to hygroscopic nature of the samples, they were stored in an exicator containing silica gel.

4.3 The quenching technique for phase diagram determination

Few of the chlorides detected in the deposits covering the samples obtained by the corrosion experiments, when simulating the conditions of the heat recovery boiler, were chosen for studying their melting behaviour. The phase boundary compositions of the binary CuCl-ZnCl₂, CuCl-FeCl₃ and FeCl₃-ZnCl₂ systems were measured by an equilibration and quenching method. This involved equilibration in isothermal conditions, a rapid quenching, and direct measurement of equilibrium phase compositions with a scanning electron microscopy. [50, 51] The thermodynamic constraints of measuring the phase diagrams are based on the Gibbs phase rule (37):

$$f = c - p + 2, \quad (37)$$

where the variable f is called the degree of freedom, c is the number of components of the system and p is the number of phases. The binary systems were measured at the constant pressure of 1 atm, thus the constant 2, representing alterable intensive variables such as temperature and pressure, is reduced to one. When the number of components (CuCl , ZnCl_2 and FeCl_3) is two in the binary systems, the phase rule shows that within a single-phase region of the phase diagram, there are two degrees of freedom. Then, temperature and composition may be varied independently and in a two-phase region, the temperature may be varied, but at any temperature, the compositions of the coexisting two phases are fixed. [52]

The experiments were conducted at isothermal conditions, reducing the f by one and resulting in a fully defined system ($f=0$). This means that changing the system composition changes only the relative amounts of the two phases, but the phase compositions of the two coexisting phases remain unchanged. The compositions of all phases in equilibrium can be determined, such as the compositions of solid phases coexisting with the liquid. [52]

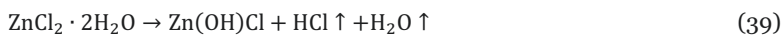
$$f = c - p + 1 = 3 - p \quad (38)$$

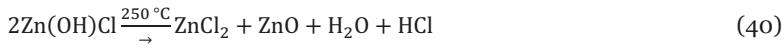
The anhydrous powders of CuCl , ZnCl_2 and FeCl_3 were used as starting materials. The samples were prepared by weighing the chloride powders before each experiment with a calibrated Mettler Toledo AB204-S semi-microbalance, that has a measurement accuracy of ± 0.1 mg, and mixing them according to predetermined starting compositions. The starting compositions were selected so that two phases could be obtained during equilibration. The sample size was small (0.4 g) in order to enhance the achievement of equilibrium and to reach higher quenching rates. The list of chemicals used and their purities are shown in Table 4.

Table 4. Starting materials used during the equilibration experiments.

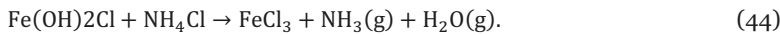
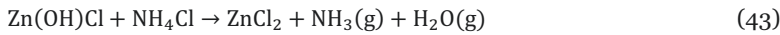
Material	Manufacturer	Purity
Zinc chloride ZnCl_2	SIGMA ALDRICH	Reagent grade $\geq 98\%$
Cuprous Chloride CuCl	SIGMA ALDRICH	Reagent grade $\geq 97\%$
Ferric Chloride FeCl_3	SIGMA ALDRICH	Reagent grade $\geq 97\%$
Ammonium Chloride NH_4Cl	SIGMA ALDRICH	99.99 %
Argon Ar	AGA	99.99 %

Despite the fact that anhydrous chlorides were used as starting materials, the anhydrous form of ZnCl_2 is highly hygroscopic, absorbing moisture rapidly from the ambient air and turning into one of five hydrates [53, 54]. It is difficult to work with anhydrous ZnCl_2 fast enough in ambient air in order to avoid hydration and if the hydrated zinc chloride is attempted to be dried by evaporating the crystalline water, oxychloride is first formed according to reactions (39) – (40). [55] FeCl_3 is highly hygroscopic as well and in exposure to air forms a series of hydrates with 2, 5 and 6 water molecules [56]. Also, when hydrated FeCl_3 is dried by heating, oxychloride is formed instead of anhydrous FeCl_3 according to reaction (41). CuCl on the other hand is fairly stable with exposure to air [57].





The sample mixtures were equilibrated in pyrex glass crucibles. In order to dry the hygroscopic chlorides, ammonium chloride was added in the bottom of the crucibles. The sample mixtures were added on top of the ammonium chloride layer so that HCl and NH₃ gases rinse the chloride powders according to reactions (42) – (44). The crucibles were covered by a lid that does not completely seal the crucible, but rather slows the rate of gas exchange with the environment so that water vapour and NH₃ gases can exit the system.



In order for ammonium chloride to dry the samples, they were first kept at 340 °C for half an hour after which the temperature was dropped to the equilibration temperature. Most chlorides are difficult to melt, because they have high vapour pressures and they volatilize at relatively low temperatures, except for the alkali and alkaline earth chlorides. For this reason, the samples were not premelted above the liquidus line.

The samples were equilibrated in a vertical electrical resistance tube furnace (Lenton CSC12/-/450V, controller by Eurotherm 3216CC) at isothermal conditions. The samples were suspended on a wire within a fused quartz work tube in the hot zone of the furnace. The location of the hot section within the work tube was located by measuring a temperature profile at 300 °C. A calibrated PT100 resistance sensor, connected to Keithley 2010 DMM multimeter (Cleveland, OH, USA), having measurement accuracy of ± 0.1 °C, was placed next to the sample for recording the sample temperature. The temperature of the hot section was measured and logged during equilibration with an NI LabVIEW temperature logging program. According to the temperature profile measurement, the uncertainty of the sample temperature was estimated to be ± 1 °C within the length of the hot zone of 8 cm. Argon was led to the furnace through a rotameter and the furnace was flushed with argon before lifting the sample to the target temperature in order to avoid oxidation. The sample was pulled to the hot section of the furnace from the bottom by pulling it on a wire from the top of the furnace. A schematic diagram of the furnace setup used for the equilibration is presented in figure 5.

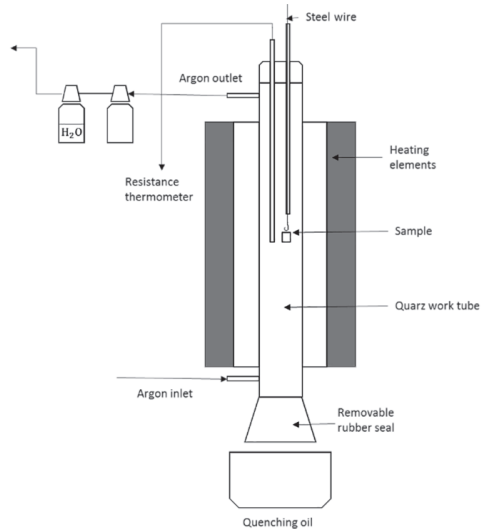


Figure 5. Schematic diagram of the furnace setup used for equilibration annealing at isothermal, isobaric experimental conditions, and for quenching.

Whether equilibrium is achieved during the annealing affects the accuracy and reliability of the results. Equilibrium conditions were confirmed by conducting equilibration experiments at the same temperature with the same sample materials, but with different equilibration times. This was done to confirm homogeneity of the phases and that no further changes occur in the sample composition as the equilibration time increases. The experimental conditions are shown in Table 5. After a sufficient time of equilibration, the samples were quenched in cooled mineral oil (Shell Ondina) due to their highly hygroscopic nature and mounted in epoxy. The sample preparation process for the SEM-EDS analysis was water-free in order to avoid contamination of the samples with moisture. The samples were polished with SiC papers P80, P240, P400, P800, P2000 and P4000, using mineral oil as lubricant to expose a suitable cross section for SEM-EDS analysis. After polishing, the oil was removed by washing in petroleum ether in an ultrasonic bath, after which they were coated with carbon (Leica EM SCD050 Coater, Leica Mikrosysteme, GmbH, Vienna).

Table 5. The experimental equilibration temperatures, starting compositions and times sufficient to reach equilibrium for the systems CuCl-ZnCl_2 , $\text{FeCl}_3\text{-ZnCl}_2$ and CuCl-FeCl_3 .

T/°C	Equilibration composition in wt%	Sufficient equilibration time /h
CuCl-ZnCl₂		
230	70 CuCl 30 ZnCl ₂	20
240	70 CuCl 30 ZnCl ₂	20
250	70 CuCl 30 ZnCl ₂	20
300	75 CuCl 25 ZnCl ₂	6
350	75 CuCl 25 ZnCl ₂	6
FeCl₃-ZnCl₂		
190	80 FeCl ₃ 20 ZnCl ₂	20
214	80 FeCl ₃ 20 ZnCl ₂	20
230	80 FeCl ₃ 20 ZnCl ₂	20
214	10 FeCl ₃ 90 ZnCl ₂	20
230	10 FeCl ₃ 90 ZnCl ₂	20
250	80 FeCl ₃ 20 ZnCl ₂	6
CuCl-FeCl₃		
307	90 CuCl 10 FeCl ₃	6
307	55 CuCl 45 FeCl ₃	6
350	90 CuCl 10 FeCl ₃	4

4.4 Scanning electron microscopy and electron dispersive spectrometry

In all the above experiments, the corroded steel samples and the compositions of phases from cross sections of quenched chloride samples, were analyzed using scanning electron microscopy and electron dispersive spectrometry (SEM-EDS). The obtained samples were analysed with a SEM LEO 1450 scanning electron microscope (Carl Zeiss Microscopy GmbH, Oberkochen, Germany) which includes an X-Max type EDS (energy dispersive spectrometer) by Oxford Instruments (Abingdon, UK). The results of the element analysis were obtained with an INCA-Energy software by Oxford Instruments. Mineral standards by Astimex Scientific limited (Toronto, Canada) were used for the EDS-analysis. INCA Energy uses the XPP matrix correction algorithm, which is a Phi-Rho-Z approach [58].

5. Thermodynamic modelling

Prediction of the chemical behaviour of multicomponent multiphase systems requires computational methods to calculate chemical equilibria between phases. When systems contain solid phases, liquid phases and gases with varying chemical compositions, the mathematical models require experimental data to fit the model to represent the real system. Often data for complex systems does not exist and a good description of the chemical behaviour in simplified systems is important for predicting systems that are more complicated.

Theoretical thermodynamic models are the basis of the CALPHAD-method (calculation of phase diagrams). In computational thermodynamics, the equilibrium state is described using thermodynamic functions that depend on temperature, pressure and composition. These computational methods are mainly based on Gibbs energy minimization of all phases. [59] The total molar Gibbs energy of a solution consists of three parts according the equation (45) [59-61].

$$G_m = G_{\text{mix}}^{\circ} + \Delta G_{\text{mix}}^{\text{ideal}} + \Delta G_{\text{mix}}^{\text{Excess}} \quad (45)$$

In which G_{mix}° represents Gibbs energy of mechanical, unreacted mixture of pure components of the system, $\Delta G_{\text{mix}}^{\text{ideal}}$ is the Gibbs energy of ideal mixing of the system and $G_{\text{mix}}^{\text{Excess}}$ is the excess Gibbs energy of mixing, which includes every other type of contribution to the Gibbs energy that is not part of mixing of the pure components, and the ideal mixing model. G_{mix}° is given by equation (46): [59, 60, 62]

$$G_{\text{mix}}^{\circ} = \sum x_i G_i^{\circ}, \quad (46)$$

where G_i° are the Gibbs energies of pure components and x_i , defined by equation (47), are the mole fractions of the components of the phase:

$$x_i = \frac{N_i}{N}, \quad (47)$$

where N_i is the number of moles of component i and N is the total number of moles of the system. [59-61]

The atomic sites within a crystal are arranged in a regular pattern called a lattice. However, the different atoms are randomly distributed. The Gibbs energy of a phase consists to two main factors, the bonding between the atoms and their configuration [61]. The ideal model for Gibbs energy of mixing, described by equations (48) - (52), is based on the assumption of random mixing referred as configurational disorder. [60] For an ideal substitutional solution the enthalpy of mixing ($\Delta H_{\text{mix}}^{\text{ideal}}$) is zero because no change in bonding energy or volume during mixing is thought to occur [59, 60, 62]

$$\Delta G_{\text{mix}}^{\text{ideal}} = \Delta H_{\text{mix}}^{\text{ideal}} - T\Delta S_{\text{mix}}^{\text{ideal}}, \quad (48)$$

where $\Delta S_{\text{mix}}^{\text{ideal}}$ is the configurational entropy of a phase. The contribution of the configurational part is the driving force for mixing of unlike atoms. The configurational entropy of a phase originates from random arrangement of atoms, derived from the Boltzmann's equation and is given by equation (49) [59, 60]

$$S = k \cdot \ln(W) = k \cdot \ln\left(\frac{N!}{N_a! \cdot N_b!}\right), \quad (49)$$

where $k = R/N_A$ is Boltzmann's constant (N_A is the Avogadro's number and R is the gas constant) and W is the number of different configurations of species A and B randomly mixed at $N=N_a+N_b$ places. Entropy for ideal mixing can now be written as (50)

$$S = \left(\frac{R}{N_A}\right) \cdot [N \cdot \ln(N) - N_a \cdot \ln(N_a) - N_b \cdot \ln(N_b)] = -R[x_a \ln(x_a) + x_b \ln(x_b)] \quad (50)$$

Identifying N_a/N and N_b/N with the mole fractions x_a and x_b we get the configurational entropy of a phase according to equation (51) and therefore the ideal Gibbs energy of mixing according to equation (52). [59-61]

$$\Delta S_{\text{mix}}^{\text{ideal}} = -R \sum_i x_i \ln x_i \quad (51)$$

$$\Delta G_{\text{mix}}^{\text{ideal}} = -RT \sum_i x_i \ln x_i \quad (52)$$

There is no enthalpy contribution in the ideal Gibbs energy of mixing, because complete random mixing is assumed. In an ideal solution, the energy of A-B interaction equals the average of the A-A and B-B interactions. The disorder will be incomplete when internal variables describing short- and long-range order are introduced. [60] The excess Gibbs energy of a multicomponent substitutional solution, expressed by equation (53), describes what remains of the real Gibbs energy of a phase when the two first terms of the equation (45) are subtracted from the total Gibbs energy of a phase. These contributions include for instance excess vibrational energy, excess configurational entropy, such as long- or short-range order, and excess enthalpy, since all enthalpy of mixing is in excess of the ideal solution behaviour etc. These contributions are used in the modelling of the real Gibbs energy of a phase by finding the best fit between the experimental results and the chosen model, through determining the suitable empirical interaction parameters of the excess part of the total molar Gibbs energy, as in [59-61]

$$\Delta G_{\text{mix}}^{\text{Excess}} = \Delta H_{\text{mix}}^{\text{Excess}} - T\Delta S_{\text{mix}}^{\text{Excess}} = \sum_{i=i}^{n-1} \sum_{j=i+1}^n x_i x_j L_{ij}, \quad (53)$$

where L_{ij} is the interaction parameter between the components of the system. The binary solution term can be extended in the composition using the differences between the site fractions of i and j according to Equation (54), which is known as the Redlich-Kister power series. [59-61]

$$L_{ij} = \sum_{n=0}^k (y_i - y_j)^n L_{ij}^n \quad (54)$$

The interaction parameter used to fit the Gibbs energy model to the experimental results, is described by the power series according to equation (55). The parameters L_{ij}^V can be temperature dependent. Normally a linear temperature dependence is enough. [60]

$$L_{ij}^n = a_{ij}^n + b_{ij}^n T \quad (55)$$

In equation (55), the composition dependence of excess enthalpy is described by a_{ij}^n and the excess entropy by b_{ij}^n [60]. Combining equations (46), (52) and (53)-(55) gives the expression for the total molar Gibbs energy of a solution according to equation (56), in which a and b are the terms of the model to be optimized to fit the experimental data.

$$G_m = \sum y_i G_i^\circ + RT \sum_i y_i \ln y_i + y_i y_j \sum_{k=0}^n (a_{ij}^n + b_{ij}^n T)^k (y_i - y_j)^k \quad (56)$$

The equation (56) describes a regular solution model where mixing is random in all directions. For more complicated applications, some mathematical alterations to terms G_{mix}° , ΔG_{mix}^{ideal} and ΔG_{mix}^{Excess} have been developed to better describe the physical properties of the molar Gibbs energy of more specific chemistries. In the following chapters, models used to describe the studied chlorides are explained.

5.1 Compound energy formalism

The compound energy formalism (CEF) is commonly used for describing the thermodynamic properties of solutions that are modelled with sublattice solution models [60, 62, 63]. Chlorides with different valences typically do not form solid solutions with one another. However, within the CuCl-ZnCl₂-FeCl₃-system solid solubilities have been detected and they were modelled using the CEF.

The majority of the solid crystalline phases have an ordered arrangement of different atoms described by a lattice. Each element prefers a particular type of lattice site. It is convenient to describe this situation by dividing the lattice into interlocking sublattices. [63] Ionic compounds such as salts consist of electrically charged components, anions and cations. Ions having the same charge repel one another while ions having opposite charges attract one another. As a result, ionic crystals exhibit strong ordering so that anions are surrounded by cations and cations are surrounded by anions in the crystal lattice. Salts can be modelled according to example lattice structure (57) where anions reside on an anionic sublattice, cations being the nearest neighbouring ions and cations reside on a cationic sublattice surrounded by anions. [62, 63]

$$(A, B)_m^{S1} (C, D)_n^{S2} \quad (57)$$

In equation (57), A, B, C and D are different elements, superscripts s1 and s2 represent different sublattices and subscripts m and n give the ratio of sites on the two sublattices. [60-63]

By selecting one constituent in each sublattice, one has a stoichiometric compound with a fixed composition. The Gibbs energy of formation of that compound contains the most important part of the bond energies. These compounds are called the end-

members of the solution phase. [61] The Gibbs energies of the end members are the main parameters of the sublattice model. [60, 63]

Let us consider the sublattice structure (57). The composition of the phase can be considered to be limited by four end-member compounds. The phase can be described by the compositions between the four end-members. [59] The end-members define the limit of solubility, but the model may have end members with a composition inside the composition range of the phase. [61] The composition surface can be represented by the equation (58), representing the Gibbs energy reference state for pure components when only the pure components exist on the sublattice. [59, 63]

$$G_{\text{mix}}^{\circ} = y_A^{S1} y_C^{S2} G_{A:C}^{\circ} + y_A^{S1} y_D^{S2} G_{A:D}^{\circ} + y_B^{S1} y_C^{S2} G_{B:C}^{\circ} + y_B^{S1} y_D^{S2} G_{B:D}^{\circ} \quad (58)$$

In equation (58) $G_{A:C}^{\circ}$, $G_{A:D}^{\circ}$, $G_{B:C}^{\circ}$ and $G_{B:D}^{\circ}$ are the Gibbs energies of the pure components AC, AD, BC and BD. To work with the sublattice model, it is necessary to define what we know as site fractions y . These are the fractional site occupations of each of the components on the various sublattices defined by equation (59)

$$y_i = \frac{N_i^s}{N}, \quad (59)$$

where N_i^s is the number of lattice sites occupied by component i on a sublattice and N is the total number of lattice sites. [60, 61, 63]

Sublattices represent a long-range order, which will modify both the entropy expression and the excess Gibbs energy. [61] Within a lattice, the distribution of different kinds of atoms on the sites is generally determined by chance to some extent. The situation is often described as chemical disorder or configurational disorder. The characteristic feature of the model is that ideal random mixing of atoms is assumed within each sublattice. This ideal configurational entropy within a sublattice is weighed with respect to the number of sites (m and n) on each sublattice. [63] Since entropy is an extensive property, which obeys the law of additivity, one could add the contributions from the individual lattices [60]. The ideal mixing contribution to the total molar Gibbs energy according to the sublattice model is given by equation (60). [59]

$$\Delta G_{\text{mix}}^{\text{ideal}} = mRT(y_A^{S1} \ln y_A^{S1} + y_B^{S1} \ln y_B^{S1}) + nRT(y_C^{S2} \ln y_C^{S2} + y_D^{S2} \ln y_D^{S2}) \quad (60)$$

The excess Gibbs energy of mixing the compounds AC, BC, AD and BD of the sublattice structure (57) is controlled by A-C, A-D, B-C and B-D interactions. Mixing on sublattices controls the A-B and C-D interaction. The interactions are compositionally dependent on the site occupation. The excess Gibbs energy of mixing is given by equation (61) [59]

$$\Delta G_{\text{mix}}^{\text{Excess}} = y_A^{S1} y_B^{S1} y_C^{S2} L_{A,B:C} + y_A^{S1} y_B^{S1} y_D^{S2} L_{A,B:D} + y_A^{S1} y_C^{S2} y_D^{S2} L_{A,C:D} + y_B^{S1} y_C^{S2} y_D^{S2} L_{B,C:D} + y_A^{S1} y_B^{S1} y_C^{S2} y_D^{S2} L_{A,B:C,D}, \quad (61)$$

where the four first terms are interaction parameters of the four binary subsystems, and the last term is a reciprocal interaction parameter. The L interaction coefficients can be temperature and composition dependent, most commonly given as Redlich-Kister terms as a function of the site fractions. The total molar Gibbs energy of a phase ($G_m = G_{\text{mix}}^{\circ} + \Delta G_{\text{mix}}^{\text{ideal}} + \Delta G_{\text{mix}}^{\text{Excess}}$) according to CEF-model is thus given by equation (62). [60, 63]

$$G_m = y_A^{S1} y_C^{S2} G_{A:C}^\circ + y_A^{S1} y_D^{S2} G_{A:D}^\circ + y_B^{S1} y_C^{S2} G_{B:C}^\circ + y_B^{S1} y_D^{S2} G_{B:D}^\circ + (mRT(y_A^{S1} \ln y_A^{S1} + y_B^{S1} \ln y_B^{S1}) + nRT(y_C^{S2} \ln y_C^{S2} + y_D^{S2} \ln y_D^{S2})) + y_A^{S1} y_B^{S1} y_C^{S2} L_{A,B:C} + y_A^{S1} y_B^{S1} y_D^{S2} L_{A,B:D} + y_A^{S1} y_C^{S2} y_D^{S2} L_{A,C:D} + y_B^{S1} y_C^{S2} y_D^{S2} L_{B,C:D} + y_A^{S1} y_B^{S1} y_C^{S2} y_D^{S2} L_{A,B,C,D} \quad (62)$$

5.1.1 CuCl-ZnCl₂ solid solution

Cu⁺ and Zn²⁺ have a different charge, which brings some complications to the requirement of electroneutrality. Replacement of two Cu⁺ ions in the solid CuCl results in the formation of cationic vacancy. In order to compensate for the charge differences between the cations, vacant cation sites were introduced to the CEF-model. The CuCl-rich solid solution of the CuCl-ZnCl₂-phase diagram was modelled according to the sublattice structure (63). [60, 63, 64]

$$(Cu^+, Zn^{2+}, Va)_1(Cl^-)_1 \quad (63)$$

The Gibbs energies of the end members are marked as (64) – (60).

$$(Cu^+)_1(Cl^-)_1 = G_{Cu^+:Cl^-}^{\circ(CuCl)} \quad (64)$$

$$(Zn^{2+})_1(Cl^-)_1 = G_{Zn^{2+}:Cl^-}^{\circ(CuCl)} \quad (65)$$

$$(Va)_1(Cl^-)_1 = G_{Va:Cl^-}^{\circ(CuCl)} \quad (66)$$

(Cu⁺)₁(Cl⁻)₁ is a solid electroneutral compound CuCl dissolving ZnCl₂ in its crystal lattice. Its Gibbs energy of formation is given by equation (67).

$$G_{Cu^+:Cl^-}^{\circ(CuCl)} = G_{CuCl}^{\circ(Solid)} \quad (67)$$

(Zn²⁺)₁(Cl⁻)₁ and (Va)₁(Cl⁻)₁ are the charged end-members. The requirement for electroneutrality is fulfilled if the site fractions of the two end-members are equal according to relation (68).

$$(Zn^{2+})_1(Cl^-)_1 + (Va)_1(Cl^-)_1 = Zn^{2+}Va(Cl^-)_2 \quad (68)$$

The Gibbs energies of these end-members were chosen to be expressed by equations (69) and (70)

$$G_{Va:Cl^-}^{\circ(CuCl)} = \frac{1}{2} G_{Cl_2}^{\circ(gas)}, \quad (69)$$

$$G_{ZnCl_2}^{\circ(CuCl)} = G_{ZnCl_2}^{\circ(Solid)} + a + bT = G_{Zn^{2+}:Cl^-}^{\circ(CuCl)} + G_{Va:Cl^-}^{\circ(CuCl)}, \quad (70)$$

where a+bT is a modelling function representing the excess Gibbs energy of the end-member. [59, 62, 63]

The excess enthalpy term a and the excess entropy term b were optimized with FactSage 7.2 thermochemical software and the following function (71) was obtained to describe the thermodynamic properties of CuCl-ZnCl₂ solid solution.

$$G_{Zn^{2+}:Cl^-}^{\circ(CuCl)} = G_{ZnCl_2}^{\circ(Solid)} - \frac{1}{2} G_{Cl_2}^{\circ(gas)} + (3165 - 29T) \quad (71)$$

5.1.2 FeCl₃-ZnCl₂ solid solution

The solid solution on the FeCl₃-rich side of the FeCl₃-ZnCl₂-phase diagram represents an opposite case to the previous copper rich solid solution of the CuCl-ZnCl₂-system. When the Fe³⁺ ions are replaced by Zn²⁺ ions, dissolving in the lattice of FeCl₃, a vacancy is formed in the anion lattice. The requirement of electroneutrality can be satisfied by the addition of vacant sites on the anion sublattice instead of the cation sublattice. The iron rich solid solution of the FeCl₃-ZnCl₂-phase diagram was modelled according to the following sublattice structure (72): [60, 63, 64]

$$(\text{Fe}^{3+}, \text{Zn}^{2+})_1(\text{Va}, \text{Cl}^-)_3 \quad (72)$$

The Gibbs energies of this sublattice structure are marked as (73)-(76):

$$(\text{Fe}^{3+})_1(\text{Cl}^-)_3 = G_{\text{Fe}^{3+}:\text{Cl}^-}^{\circ(\text{FeCl}_3)} \quad (73)$$

$$(\text{Fe}^{3+})_1(\text{Va})_3 = G_{\text{Fe}^{3+}:\text{Va}}^{\circ(\text{FeCl}_3)} \quad (74)$$

$$(\text{Zn}^{2+})_1(\text{Cl}^-)_3 = G_{\text{Zn}^{2+}:\text{Cl}^-}^{\circ(\text{FeCl}_3)} \quad (75)$$

$$(\text{Zn}^{2+})_1(\text{Va})_3 = G_{\text{Zn}^{2+}:\text{Va}}^{\circ(\text{FeCl}_3)} \quad (76)$$

(Fe³⁺)₁(Cl⁻)₃ represents the solid electroneutral compound FeCl₃ and its Gibbs energy is defined by equation (77).

$$G_{\text{Fe}^{3+}:\text{Cl}^-}^{\circ(\text{FeCl}_3)} = G_{\text{FeCl}_3}^{\circ(\text{Solid})} \quad (77)$$

The rest of the end-members are charged species. Gibbs energy for the charged end-member (Zn²⁺)₁(Va)₃ was chosen to be defined according to equation (78).

$$G_{\text{Zn}^{2+}:\text{Va}}^{\circ(\text{FeCl}_3)} = G_{\text{ZnCl}_2}^{\circ(\text{Solid})} - G_{\text{Cl}_2}^{\circ(\text{gas})} \quad (78)$$

The requirement for electroneutrality is satisfied by the expression (79).

$$\frac{2}{3}(\text{Zn}^{2+})_1(\text{Cl}^-)_3 + \frac{1}{3}(\text{Zn}^{2+})_1(\text{Va})_3 = \text{Zn}^{2+}\text{Va}(\text{Cl}^-)_2 \quad (79)$$

Thus, the Gibbs energy of the end-member (Zn²⁺)₁(Cl⁻)₃ can be obtained by equation (80).

$$G_{\text{ZnCl}_2}^{\circ(\text{FeCl}_3)} = G_{\text{ZnCl}_2}^{\circ(\text{Solid})} + a + bT = \frac{2}{3}G_{\text{Zn}^{2+}:\text{Cl}^-}^{\circ(\text{FeCl}_3)} + \frac{1}{3}G_{\text{Zn}^{2+}:\text{Va}}^{\circ(\text{FeCl}_3)} + 3RT \left[\frac{2}{3} \ln \left(\frac{2}{3} \right) + \frac{1}{3} \ln \left(\frac{1}{3} \right) \right] \quad (80)$$

Optimized parameters for excess enthalpy *a* and the excess entropy *b* are given by equation (81).

$$G_{\text{Zn}^{2+}:\text{Cl}^-}^{\circ(\text{FeCl}_3)} = G_{\text{ZnCl}_2}^{\circ(\text{Solid})} + \frac{1}{2}G_{\text{Cl}_2}^{\circ(\text{gas})} + \frac{3}{2}(7455 - 17T) - 3RT \left[\frac{2}{3} \ln \left(\frac{2}{3} \right) + \frac{1}{3} \ln \left(\frac{1}{3} \right) \right] \quad (81)$$

Gibbs energy for the last charged end-member (Fe³⁺)₁(Va)₃ can now be solved from the reciprocal reaction (82) by inserting the Gibbs energies of the already solved Gibbs energies of the rest of the end-members (77), (78) and (80). [60, 63, 64]

$$G_{\text{Fe}^{3+}:\text{Va}}^{\circ(\text{FeCl}_3)} + G_{\text{Zn}^{2+}:\text{Cl}^-}^{\circ(\text{FeCl}_3)} = G_{\text{Fe}^{3+}:\text{Cl}^-}^{\circ(\text{FeCl}_3)} + G_{\text{Zn}^{2+}:\text{Va}}^{\circ(\text{FeCl}_3)} \quad (82)$$

Solving equation (82) gives the Gibbs energy of the end-member $(\text{Fe}^{3+})_1(\text{Va})_3$ according to equation (83).

$$G_{\text{Fe}^{3+},\text{Va}}^{\circ(\text{FeCl}_3)} = G_{\text{FeCl}_3}^{\circ(\text{Solid})} - \frac{3}{2} G_{\text{Cl}_2}^{\circ(\text{gas})} - \frac{3}{2} (7455 - 17T) + 3RT \left[\frac{2}{3} \ln \left(\frac{2}{3} \right) + \frac{1}{3} \ln \left(\frac{1}{3} \right) \right] \quad (83)$$

5.1.3 ZnCl₂-FeCl₃ solid solution

The solid solution on the ZnCl₂-rich side of the FeCl₃-ZnCl₂-phase diagram was modelled according to sublattice structure (84): [60, 63, 64]



in which the end-member compounds and their Gibbs energies are marked according to (85)-(87):

$$(\text{Zn}^{2+})_1(\text{Cl}^-)_2 = G_{\text{Zn}^{2+},\text{Cl}^-}^{\circ(\text{ZnCl}_2)} \quad (85)$$

$$(\text{Fe}^{3+})_1(\text{Cl}^-)_2 = G_{\text{Fe}^{3+},\text{Cl}^-}^{\circ(\text{ZnCl}_2)} \quad (86)$$

$$(\text{Va})_1(\text{Cl}^-)_2 = G_{\text{Va},\text{Cl}^-}^{\circ(\text{ZnCl}_2)} \quad (87)$$

The end-member $(\text{Zn}^{2+})_1(\text{Cl}^-)_2$ is the solid electroneutral compound ZnCl₂ and its Gibbs energy of formation is given by equation (88).

$$G_{\text{Zn}^{2+},\text{Cl}^-}^{\circ(\text{ZnCl}_2)} = G_{\text{ZnCl}_2}^{\circ(\text{Solid})} \quad (88)$$

$(\text{Fe}^{3+})_1(\text{Cl}^-)_2$ and $(\text{Va})_1(\text{Cl}^-)_2$ are charged end-members, for which the requirement of electroneutrality is satisfied by relation (89).

$$(\text{Fe}^{3+})_1(\text{Cl}^-)_2 + \frac{1}{2}(\text{Va})_1(\text{Cl}^-)_2 = \text{Fe}^{3+} \frac{1}{2} \text{Va}(\text{Cl}^-)_3 \quad (89)$$

Thus, Gibbs energies for the end-members $(\text{Va})_1(\text{Cl}^-)_2$ and $(\text{Fe}^{3+})_1(\text{Cl}^-)_2$ are defined by equations (90) and (91). [60, 63, 64]

$$G_{\text{Va},\text{Cl}^-}^{\circ(\text{ZnCl}_2)} = G_{\text{Cl}_2}^{\circ(\text{gas})} \quad (90)$$

$$G_{\text{FeCl}_3}^{\circ(\text{ZnCl}_2)} = G_{\text{FeCl}_3}^{\circ(\text{Solid})} + a + bT = G_{\text{Fe}^{3+},\text{Cl}^-}^{\circ(\text{ZnCl}_2)} + \frac{1}{2} G_{\text{Fe}^{3+},\text{Va}}^{\circ(\text{ZnCl}_2)} + RT \left[\frac{1}{2} \ln \left(\frac{1}{2} \right) \right] \quad (91)$$

The optimized excess enthalpy and entropy parameters for the Gibbs energy of formation of the $(\text{Fe}^{3+})_1(\text{Cl}^-)_2$ end-member are given by equation (92).

$$G_{\text{Fe}^{3+},\text{Cl}^-}^{\circ(\text{ZnCl}_2)} = G_{\text{FeCl}_3}^{\circ(\text{Solid})} - \frac{1}{2} G_{\text{Cl}_2}^{\circ(\text{gas})} + (6746 - 12T) - RT \left[\frac{1}{2} \ln \left(\frac{1}{2} \right) \right] \quad (92)$$

5.2 Quasi-chemical model

Molten salts typically have a tendency for strong chemical ordering, where the cations tend to surround themselves with anions and vice versa due to the Coulomb forces. In addition, many ionic systems show strong short-range ordering, where cation-cation and anion-anion pairs are second nearest neighbours. The quasi-chemical model takes

into account non-random mixing between A and B atoms, forming AA, BB and AB pairs. The formation of the bonds is described by a simple chemical reaction formula that can be written as the Gibbs energy change of the reaction for the molecules AA, BB and AB. The model is based upon the assumption that the energy of the whole system is the sum of the bond energies between neighbouring atoms. The formation of a chloride solution from the pure components can be regarded as a chemical reaction between different kinds of bonds, similar to the reaction between molecules according to equation (93)

$$(A - Cl - A)_{\text{pair}} + (B - Cl - B)_{\text{pair}} = 2(A - Cl - B)_{\text{pair}} \quad \Delta g_{AB/Cl}, \quad (93)$$

where $\Delta g_{AB/Cl}$ is a modelling parameter representing the non-configurational Gibbs energy change of the cation-cation pair formation. [60, 61, 65–71]

The liquid has a strong tendency to order around specific compositions. The extent of short-range ordering of the solution is determined by calculating the equilibrium amount of the second-nearest-neighbour (cation-cation) pairs formed according to reaction (93). [65–71] In the case of chloride systems, the anion sublattice only contains chlorine, which is why the model only considers formations and mixing of cation-cation pairs on the cation sublattice [64].

A positive $\Delta g_{AB/Cl}$ value indicates that AA and BB pairs are dominant in the solution. A negative $\Delta g_{AB/Cl}$ value on the other hand would favour the formation of AB pairs, meaning that the system has a tendency of forming compounds and becoming more ordered. $\Delta g_{AB/Cl}$ of equation (93) is given by equation (94) [60, 65–68]

$$\Delta g_{AB/Cl} = \Delta g_{AB}^0 + \sum_{i \geq 1} g_{AB}^{i0} Y_A^i + \sum_{j \geq 1} g_{AB}^{0j} Y_B^j, \quad (94)$$

in which g_{AB}^0 , g_{AB}^{i0} and g_{AB}^{0j} are the model parameters expressed in a polynomial form ($a+bT$) so that a and b are optimized to fit the experimental data. [65–68] If the molar enthalpy and entropy change of this reaction, denoted by a and b in $a+bT$, is zero, the solution is ideal. However, if $a+bT$ is negative then there will be ordering of the mixture at around the 50:50 composition and the enthalpy and entropy of mixing will show a distinct minimum at the AB composition. As ordering does not always occur at AB it is desirable to allow other compositions to be chosen for the position of the minima, which is done by replacing mole fractions with equivalent site fractions Y_A and Y_B expressed by equations (95)–(96) [59]

$$Y_A = Z_A Y_A / (Z_A X_A + Z_B X_B), \quad (95)$$

$$Y_B = Z_B Y_B / (Z_A X_A + Z_B X_B), \quad (96)$$

where Z_A and Z_B are coordination numbers of cations A and B, and X_A and X_B are the site fractions in the sublattice. [64–71]

The total molar Gibbs energy of a solution phase according to the quasi-chemical model $G_m = G_{\text{mix}}^0 + \Delta G_{\text{mix}}^{\text{ideal}} + \Delta G_{\text{mix}}^{\text{Excess}}$ is given by equation (97) [65–68]

$$G_m = (n_A G_A^0 + n_B G_B^0) - T \Delta S^{\text{ideal}} + \frac{n_{AB}}{2} \Delta g_{AB}, \quad (97)$$

where $n_A G_A^0$ and $n_B G_B^0$ are the molar Gibbs energies of the pure components. ΔS^{ideal} is the configurational entropy of mixing given by randomly distributing the (A-A), (B-B),

and (A-B) pairs, expressed by equation (98), and $\frac{n_{AB}}{2} \Delta g_{AB}$ is the excess Gibbs energy of mixing, in which n_{AB} is the number of pairs between cations A and B.

$$\Delta S^{\text{Ideal}} = -R(n_A \ln X_A + n_B \ln X_B) - R \left[n_{AA} \ln \frac{X_{AA}}{Y_A^2} + n_{BB} \ln \frac{X_{BB}}{Y_B^2} + n_{AB} \ln \frac{X_{AB}}{2Y_A Y_B} \right] \quad (98)$$

where, n_{AA} , n_{BB} and n_{AB} are the total number of pairs in the solution. [65-68]

To model the liquid binary solutions of the CuCl-CuCl₂-FeCl₂-FeCl₃-ZnCl₂-PbCl₂-system the following coordination numbers for Z_A and Z_B were chosen according to the relations (99)-(101).

$$Z_A^X = 6, Z_{Cl}^X = 3 \quad (99)$$

$$Z_B^Y = 6, Z_{Cl}^Y = 6 \quad (100)$$

$$Z_C^Z = 6, Z_{Cl}^Z = 2 \quad (101)$$

$$X = MCl_2, Y = MCl, Z = MCl_3$$

$$A = Zn^{2+}, Fe^{2+}, Cu^{2+}, Pb^{2+}, B = Cu^+, C = Fe^{3+}$$

The ratio between the second nearest neighbours N_{SNN} and the first nearest neighbours N_{FNN} for each component was assumed to be constant. This ratio ζ was described by equation (102) and was given a value 2.4. [62]

$$\frac{N_{SNN}}{N_{FNN}} = \frac{\zeta}{2} \quad (102)$$

The excess Gibbs energies describing the liquid binary solutions of the CuCl-CuCl₂-FeCl₂-FeCl₃-ZnCl₂-PbCl₂ system are presented in Table 6.

Table 6. Optimized interaction parameters for the liquid phase of the CuCl-CuCl₂-ZnCl₂-FeCl₂-FeCl₃-PbCl₂-system.

$\Delta g_{Cu(+), Zn(2+)/Cl} \left(\frac{J}{mol} \right) = (3960.7 - 3.7732T) - 2018.3\chi_{Cu} - (4457.2 - 0.783T)\chi_{Zn}$
$\Delta g_{Fe(3+), Zn(2+)/Cl} \left(\frac{J}{mol} \right) = -3865 + 634\chi_{Fe} - 5687\chi_{Zn}$
$\Delta g_{Cu(+), Fe(3+)/Cl} \left(\frac{J}{mol} \right) = -4364 + (2940 + 3.24T)\chi_{Cu} - 1534\chi_{Fe}$
$\Delta g_{Fe(3+), Fe(2+)/Cl} \left(\frac{J}{mol} \right) = -4855 + 4.19T$
$\Delta g_{Fe(2+), Cu(2+)/Cl} \left(\frac{J}{mol} \right) = -2191$
$\Delta g_{Cu(+), Pb(2+)/Cl} \left(\frac{J}{mol} \right) = -360.8 - 798.8\chi_{Pb(2+)}$

6. Results and discussion

6.1 Corrosion mechanism within the heat recovery boiler

Based on the hot corrosion experiments simulating the conditions of the heat recovery boiler, the key factor enabling corrosion damage of high alloy steels in the operating temperature range (250 °C-350 °C) of the boiler steel walls, was considered to be melting of the copper smelter flue dust deposit. Corrosion products of the steels alloying elements were found in the scale/dust deposit at those locations, where the dust deposit seemed to have been melted and contacted the steel. Where the steel surface was not covered by the molten deposit, no corrosion damage was observed. Addition of ZnCl_2 to the copper smelter flue dust (composed mainly of sulphates and oxides of Cu, Fe, Zn and Pb) resulted in melting of the copper smelter flue dust deposit at the temperature range of 250 °C – 350 °C based on visual observations, an example of which is given in Figure 6. The reference deposit of copper smelter flue dust without ZnCl_2 addition, did not have contact with the steel surface and the dust particles were clearly separated from each other as shown in Figure 6b.

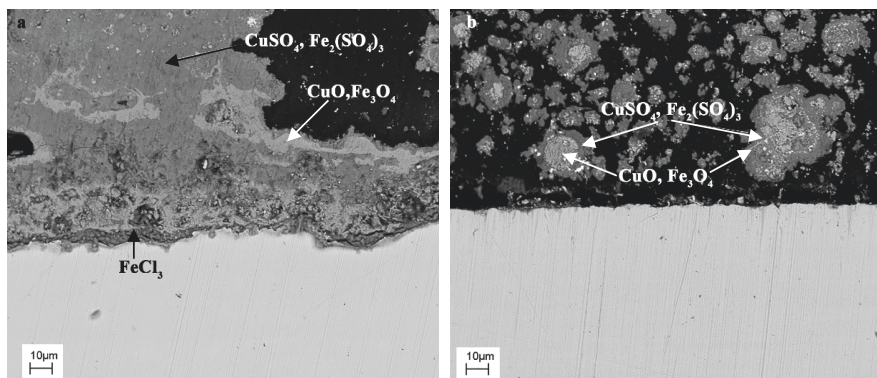
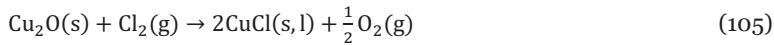
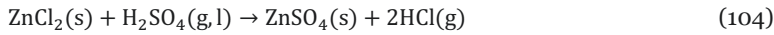
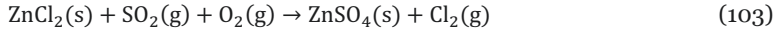


Figure 6. Figure a represents a scanning electron microscope image of a cross section of the surface of P235GH carbon steel covered by copper smelter flue dust deposit containing added ZnCl_2 after two weeks of exposure at 250 °C in $\text{SO}_2\text{-N}_2\text{-O}_2\text{-H}_2\text{O}$ atmosphere. Figure b represents a cross section of the same steel in the same experimental conditions without addition of ZnCl_2 .

Corrosion by molten salts is much more aggressive than compared to the solid state corrosion due to larger contact area between the molten salt mixture and the steels oxide scale [32, 35, 38 39, 72,73]. When the deposit of oxides, chlorides and sulphates melts, the ionic components (SO_4^{2-} , Cl^- , O^{2-} , Cu^{2+} , Zn^{2+} etc.) composing the salts become more mobile resulting fast diffusion rates, since molten salts are good ionic conductors. [32, 36, 38, 39, 45]

HSC 8.1 calculations comparing the Gibbs energies of sulphating reactions of chlorides and chlorination reactions of oxides shown in Figure 7, suggest the following sequence of reactions within the dust deposit: During the corrosion experiments, chlorine originating from the ZnCl_2 in the copper smelter flue dust deposit, reacted with Cu_2O forming CuCl . Absence of large amounts of ZnCl_2 in the deposit suggests that SO_2 , O_2 , SO_3 and H_2SO_4 gases in the furnace atmosphere reacted with the ZnCl_2 converting it to ZnSO_4 and releasing chlorine according to reactions (103) and (104), which then reacted with the copper oxide according to reaction (105). SO_3 is more stable at the temperature range of this study, but SO_2 and O_2 are more abundant.



The chlorine released by sulphation of ZnCl_2 should react with the Cu_2O rather than with CuSO_4 because the Gibbs energy of copper sulphate reacting with chlorine to CuCl is positive. However, reactions of copper oxides with chlorine to CuCl have negative Gibbs energies. Sulphation of chlorides are energetically favoured reactions, and chlorine is released within the deposit to react with oxides of Cu, Pb and Zn, to form chlorides.

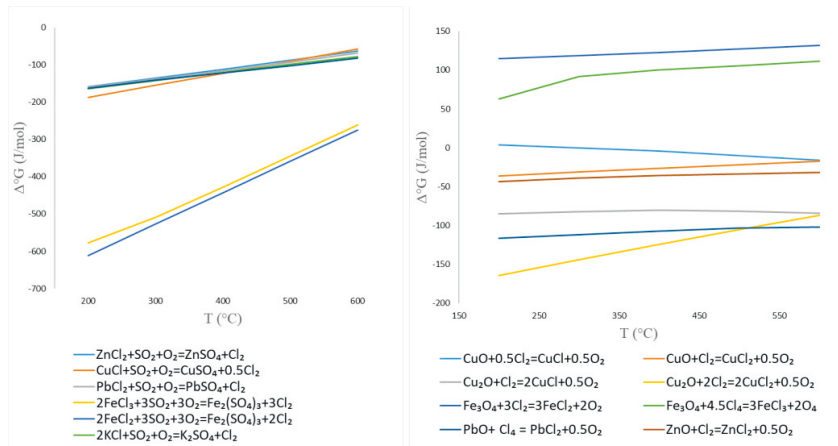


Figure 7. Gibbs energies of sulphation reactions of chlorides and chlorination reactions of oxides calculated by HSC version 8.1 using database MainDB8.

CuCl was found most abundantly in the copper smelter flue dust deposit compared to other chlorides. In addition to CuCl , varying chlorine concentrations were measured everywhere in the deposit, where melt seemed to have formed. The process gas within the boiler contains SO_2 , O_2 , SO_3 , H_2O and H_2SO_4 gases that diffuse into the accretion layer. Within the dust deposit, chlorides of the dust react to sulphates and locally HCl and Cl_2 gases are likely to be formed as a result of the sulphation reactions of chlorides in the dust. According to Miettinen [2] et al. the source of chlorine in the deposit originates from condensing vapours that form a sticky coating on the boiler walls at temperatures of around 500 °C, near the melting point of eutectics of the NaCl-KCl -

Na_2SO_4 - K_2SO_4 -system. Most common metals in the copper smelter flue dust are Cu, Fe, Zn and Pb. When the copper ores contain chlorine, the oxides of these metals within the flue dust deposit may react with the chlorine released by sulphation of the alkali chlorides and form chlorides of CuCl , ZnCl_2 , PbCl_2 etc., which would dramatically reduce the melting point of the deposit.

In order to study the effect of heavy metal chlorides on the melting behaviour of the copper smelter flue dust, binary phase diagrams of the CuCl - CuCl_2 - FeCl_2 - FeCl_3 - ZnCl_2 - PbCl_2 -system were studied experimentally by equilibration-quenching method and scanning electron microscopy. The phase diagrams were optimized using the CALPHAD-technique incorporating and evaluating all available phase diagram data concerning these systems [74-80]. The liquid salt solutions were modelled according to the modified quasi-chemical model and the solid solutions were modelled according to the compound energy formalism described in chapter 5. The measured and optimized phase diagrams are presented in Figures 8 - 11. A detailed description of the analysis of the results is presented in Article 4.

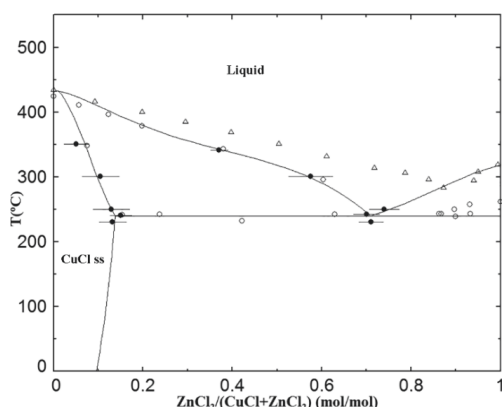


Figure 8. The calculated equilibrium phase diagram of the CuCl - ZnCl_2 -system compared with the experimental data. Experimental data are from Hermann et al [74] (\circ), Palkin et al [75] (Δ) and this study (\bullet).

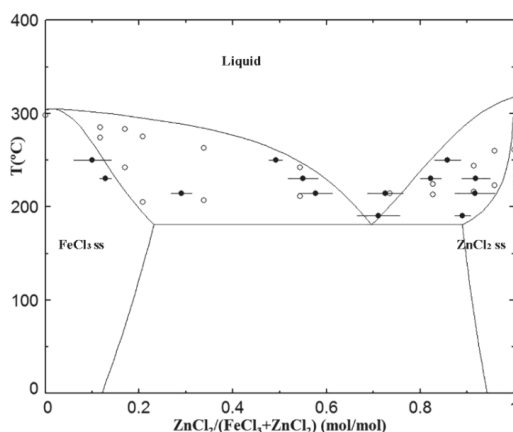


Figure 9. The calculated equilibrium phase diagram of the FeCl_3 - ZnCl_2 -system compared with experimental results. Experimental data are from Hermann et al [74] (\circ) and this study (\bullet).

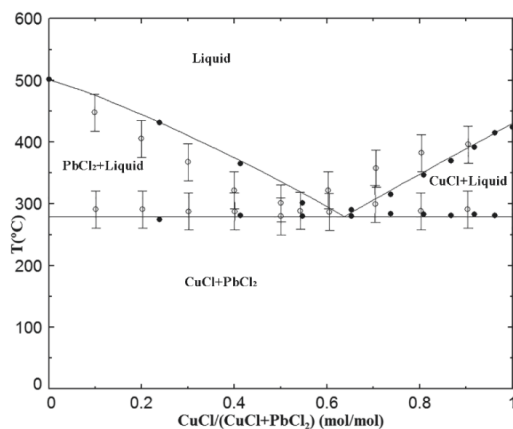


Figure 10. The calculated equilibrium phase diagram of the CuCl-PbCl₂-system compared with experimental results. Experimental data are from Hermann et al. [74] (●) and from Coleman et al. [76] (○) with error bars included.

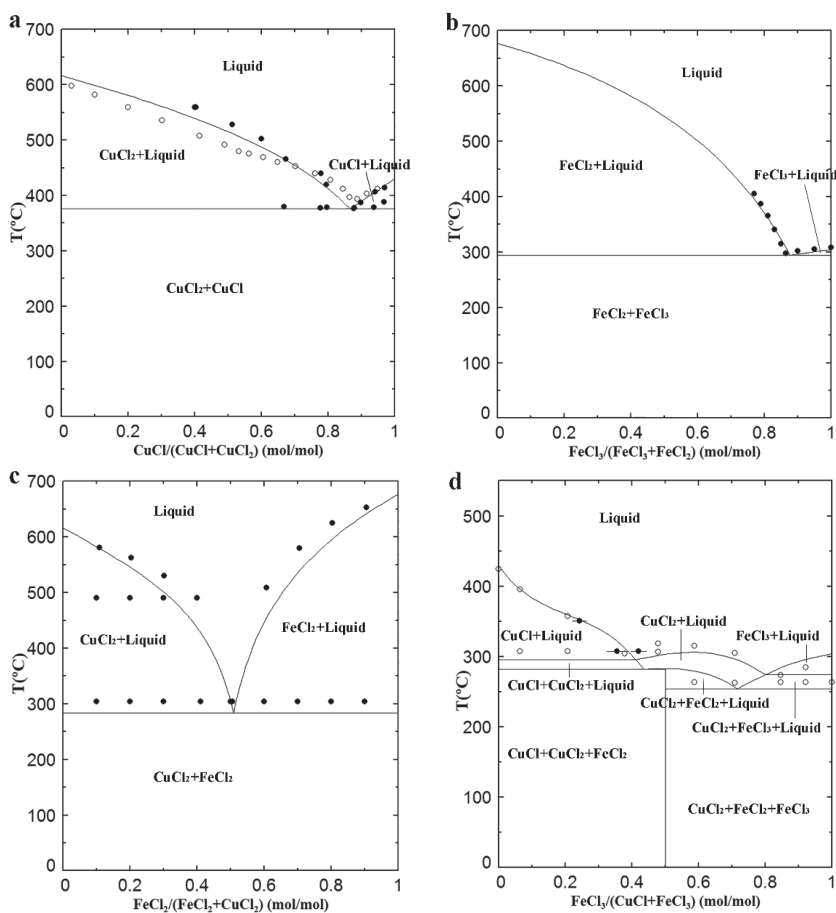


Figure 11. The calculated equilibrium phase diagrams of the CuCl₂-CuCl, FeCl₂-FeCl₃, CuCl₂-FeCl₂ and CuCl-FeCl₃-systems compared with experimental data. Experimental data in figure a are from Biltz et al. [77] (○) and Safonov et al. [78] (●). Experimental data in figure b are from Schäfer et al. [79] (●). Experimental data in figure c are from Korzhukov et al. [80] (●). Experimental data in figure d are from this study (●) and from Hermann et al. [74] (○).

Figures 6 and 7 show that if ZnCl_2 , CuCl , and FeCl_3 chlorides are formed within the dust deposits and if these chlorides come in contact with each other, a molten phase is formed even at the lowest operating temperatures, around 250 °C, of the heat recovery boiler walls resulting in hot corrosion.

6.2 Hot corrosion of carbon steel in the conditions of the heat recovery boiler

A part of the heat recovery boiler walls of Boliden Harjavalta copper smelter are made of carbon steel tubes clad by stainless steel for corrosion resistance. Damage to the stainless steel coating would result in fast corrosion rate of the boiler. The corrosion damage of the carbon steel reveals the fundamental hot corrosion mechanism of the steel surface in SO_2 - SO_3 - H_2SO_4 - H_2O - O_2 - N_2 atmosphere under the copper smelter flue dust deposit without interference of the steels alloying elements that provide protection against corrosion.

As a result of the corrosion experiments, a layered scale structure grew on the carbon steel surface under the sulphate and chloride deposit. $\text{FeCl}_2/\text{FeCl}_3$ scale was detected on the steel surface and beneath it as pitting corrosion damage. In addition, oxides of iron were found at the steel surface together with chlorides and in pitting corrosion areas. With rising temperature the mixed FeCl_2 and Fe_2O_3 layer covering the steel surface grows thicker, and at 350 °C the chloride pits disappear most likely due to formation of gaseous $(\text{FeCl}_3)_2$. Typically, a Fe_2O_3 layer was found top of the oxide and chloride scale. On top of the hematite layer, sulphate scale composed of $\text{Fe}_2(\text{SO}_4)_3$ formed adjacent to the gas phase. In addition, sulphates of zinc and copper were found among the iron sulphate. With rising temperature, the hematite layer in the middle of the scale begins to disappear by reacting to sulphate and eventually the scale consists of a thick mixed oxide and chloride layer covered by sulphate scale. Figure 12 shows the development of the scales grown on the carbon steel between temperatures of 250 °C - 350 °C with and without ZnCl_2 addition to the deposit.

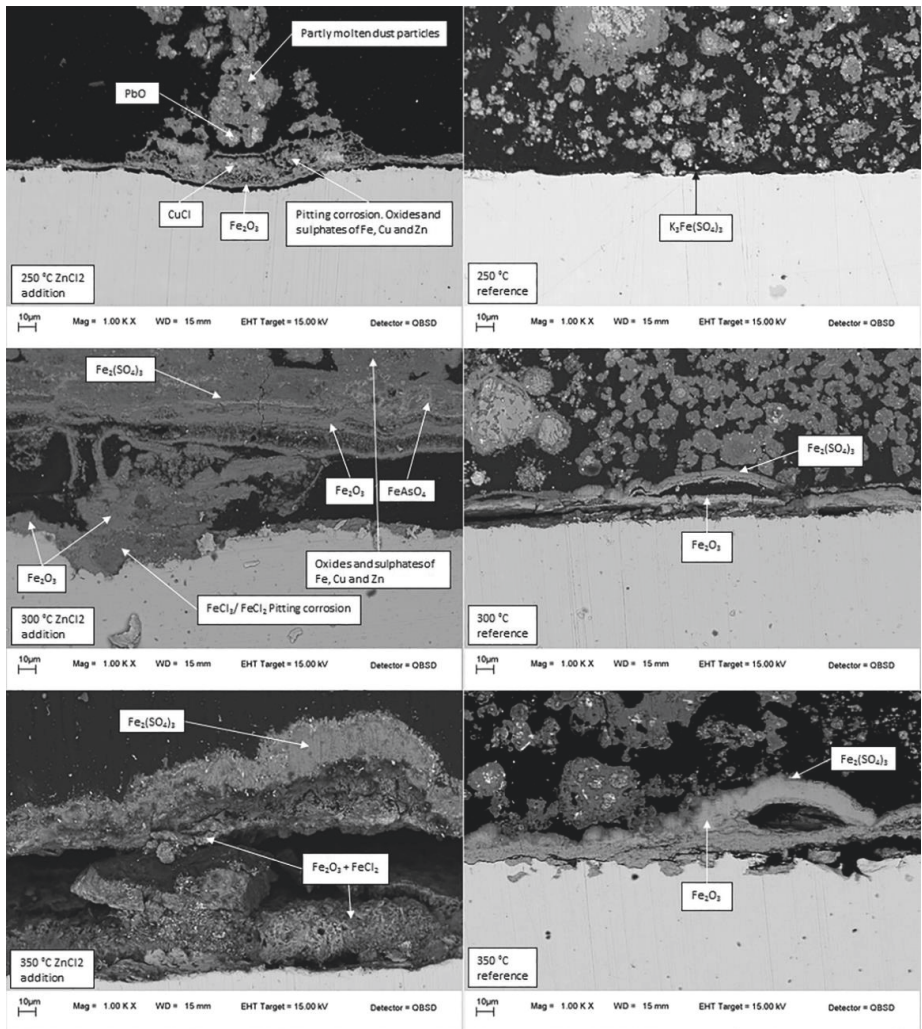


Figure 12. Development of the scale structure of P235GH carbon-steel as a function of temperature. The steel surface was exposed to deposit containing 65 wt% of copper smelter flue dust with added 5 wt% KCl and 30 wt% ZnCl_2 after two weeks of exposure at 250 °C - 350 °C in 43 vol% SO_2 , 39 vol% N_2 , 9 vol% O_2 and 9 vol % H_2O atmosphere. In the reference condition, the steel surface was exposed to deposit composition of 95 wt% copper smelter flue dust and 5 wt% KCl in otherwise the same test conditions.

Based on the above observations a general corrosion mechanism of steel beneath the chloride and sulphate deposit can be proposed: Hot corrosion of steel starts by dissociation of the sulphate anion to acidic and basic component when coming into contact with the oxide surface. Bases are O^{2-} donors while acids are O^{2-} acceptors. During melting of the deposit, sulphate ion SO_4^{2-} dissociates according to reactions (106) and (107). Basicity of the melt is defined by its oxygen ion activity. Oxygen from the surrounding atmosphere also dissolves in the melt and reduces according to reaction (108). [81] Electrons for the cathodic reduction of oxyanions are provided by anodic metal dissolution on the steel surface according to reaction (109) and their conduction through the oxide scale towards the melt [82].



Increasing O^{2-} activity of the melt at the oxide surface results in oxide dissolution according to reaction (110) [81]. The concentration gradient between acidic SO_3^{2-} -rich melt surface and the basic MO_2^{2-} -rich oxide surface pulls these components towards each other forming sulphates according to reaction (111) [17]. For this reason, sulphate scale forms above the oxide scale. Disappearance of the middle oxide layer of the scale with rising temperature indicates that the oxide scale is dissolved by the sulphate melt by basic fluxing mechanism at 350 °C when the reaction rates become faster.



Since sulphur dioxide and oxygen were present in the system with chloride compounds, sulphur dioxide acted as an initiator for chloride induced corrosion, by reacting with ZnCl_2 and KCl in the dust deposit transforming them into sulphates. At the same time, chlorine was released for the reactions with the steel and the oxides in the copper smelter flue dust. Released Cl_2 and HCl dissociate to ions according to reactions (112) and (113). Chlorides of the steels alloying metals were always formed close to the steel surface and below it, which means that chemical potential difference between the oxide surface and steel surface pulls Cl^- ions towards the steel surface through oxide defects [48, 83].



On the oxide/steel interface, oxygen has been consumed by oxide formation resulting in a low oxygen partial pressure on the steel surface. As Cl^- ions gather at the oxide/steel interface, high partial pressures of chlorine are created on the steel surface. Low partial pressures of oxygen and high partial pressures of chlorine enables formation of chlorides according to reaction (114). [32, 34, 35, 37-39, 43, 45-48, 84]

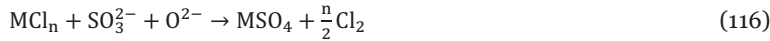


Chlorides as well as oxides were discovered together in the scale structure adjacent to the steel surface. According to Jonsson et al. [82] chloride precipitation is connected to formation of voids in the steel. Pore formation takes place above the steel grain boundaries, where chlorides nucleate. Transition metal chlorides are poor electronic conductors and the chlorination of the steel surface would stop if, a continuous chloride scale was formed. Iron oxides grow inwards and outwards from the steel surface in areas where chloride precipitates are not present and where the steel has electronic contact with the oxide scale. [82] The growth of the oxides and chlorides in the corro-

sion pit may be possible by basic dissolution of the chlorides followed by oxide formation, which releases chlorine inside the pit enabling its growth according to reaction (115) [30].



The chlorides diffuse easily towards the scale surface due to their high vapour pressures even at low temperatures, resulting in rapid metal loss from the steel surface. Sulphur and oxygen partial pressures increase with increasing distance from the steel surface, leading to sulphation and oxidation of the chlorides, contributing to further scale growth. The resulting sulphates and oxides formed through reactions (116) – (118) form a porous and loose scale, providing no protective properties against oxidation. [32, 34, 35, 37-39, 43, 45-48, 84] The pores provide fast diffusion pathways for chlorides towards higher SO_2 and O_2 partial pressures in the scale.



By the above reactions, gaseous chlorine is released again and it diffuses to the bulk gas forming HCl or back to the metal surface establishing a chlorine cycle [32, 34, 35, 37-40, 43, 45-48, 84]. A diagram illustrating the corrosion mechanism based on the cycles of chlorine and sulphur is shown in Figure 13.

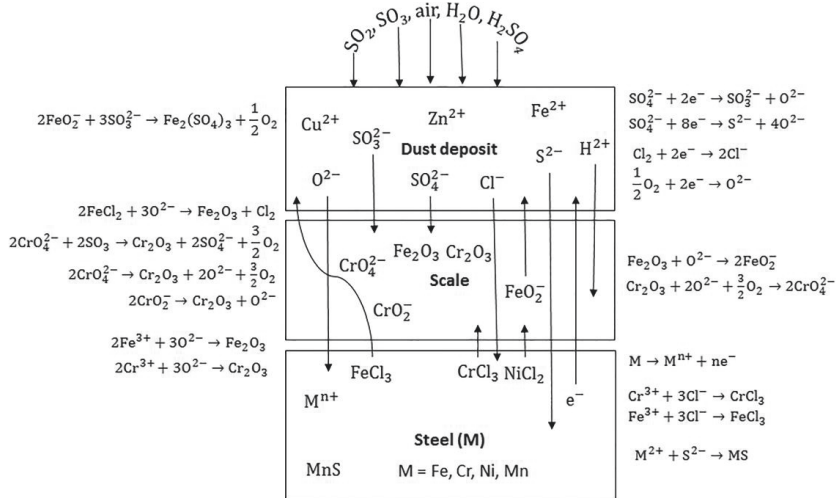


Figure 13. Schematic pattern of the corrosion mechanism of steel in the environment of heat recovery boiler of copper flash smelting process based on the cycles of sulphur and chlorine in the dust deposit and oxide scale beneath.

When the high alloy boiler steels were exposed to the experimental conditions, protective Cr_2O_3 scale did not form on the steel surface. Instead, a corrosion layer composed of oxides and chlorides of iron, chromium and nickel formed above the steel surface, which was covered by the sulphate deposit. Only small concentrations (few

wt%) of chromium and nickel were generally found in the molten sulphate layer indicating that CrCl_3 and NiCl_2 are not very soluble in the heavy metal sulphate melt. In the following chapters, chromium, nickel and molybdenum alloying of the steel in terms of their role as building the corrosion resistance of the steel are discussed when exposed to copper smelter flue dust accretions. High chromium stainless steel AISI 304 was studied to learn about the hot corrosion resistance by chromium alloying, Sanicro 28 was studied to test the effects high nickel and chromium alloying and AISI 316 to differentiate the effect of molybdenum alloying.

Due to the chemical complexity of the copper smelter flue dust, identification of chemical compositions of corrosion products and the dust was difficult. The interpretations of the corrosion products and dust components are based on FactSage calculations of the elements obtained from the EDS-spectra. Elements occurring over 10 wt% concentrations in the spectra are included in the interpretation of the corrosion products. In general, the samples were challenging to analyze. They were porous, hygroscopic, and fragile under the electron beam. For this reason, their quantitative analysis was not possible and FactSage was also utilized to help with the interpretation of the EDS-analysis by calculating which phases composed of the identified elements would be thermodynamically stable and most likely to form in the circumstances of the experiments.

6.3 Corrosion resistance of AISI 304: The effect of Chromium alloying in the conditions of the heat recovery boiler

Chromium is considered the most effective alloying element to prevent hot corrosion under molten sulphates, which was demonstrated by the fact that only small concentrations of chromium were detected uniformly in the molten sulphate deposit. Good hot corrosion protection of Cr_2O_3 is based on its good stability under molten sulphates. Even though Cr_2O_3 undergoes basic dissolution under molten sulphate deposit according to reaction (119) producing chromate anions to the melt, Cr_2O_3 starts forming at much lower oxygen partial pressures compared to the other oxides of the steels alloying metals. [29, 85]



The chromate anions may be reduced in preference to sulphate anions according to reactions (120) - (122), because their reduction takes place at much lower reducing potentials than required for reduction of sulphate anions according to reactions (106) and (107). [29, 85]



Formation of chromate anions shifts the melt basicity and oxygen partial pressure to the Cr_2O_3 stability range, which results in precipitation of chromate anions as Cr_2O_3 . Due to the wide stability range of Cr_2O_3 as a function of oxygen partial pressure, chromite anions also precipitate as Cr_2O_3 at higher SO_2 partial pressures compared to other

alloying elements of steel, but also at locally reducing sites such as grain boundaries, where oxygen partial pressure is low, according to reactions (123) - (125). If the extent of Cr_2O_3 precipitation is adequate, the steel surface can be protected from the molten salt. [29, 85] The wide stability range of Cr_2O_3 as a function of SO_2 , O_2 and Cl_2 is shown in Figure 14.

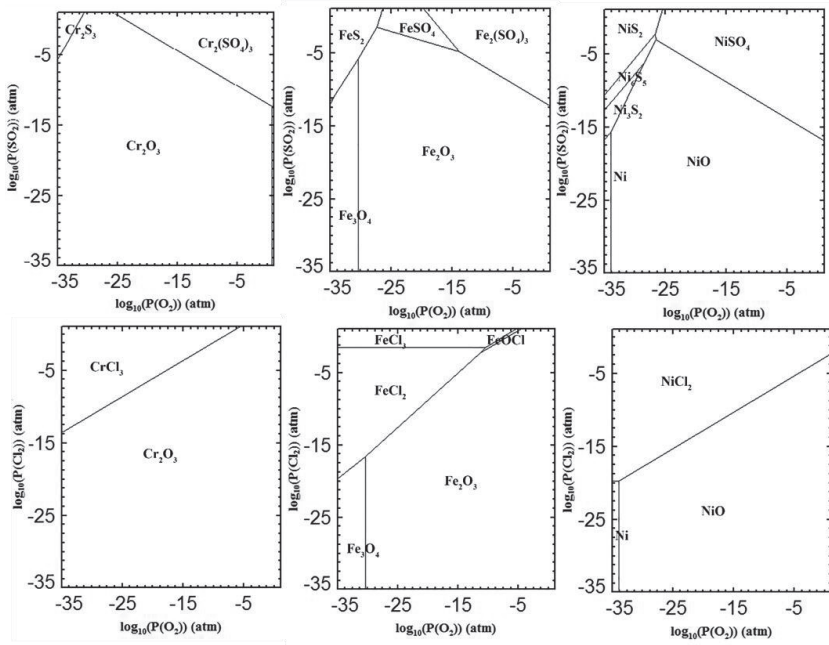
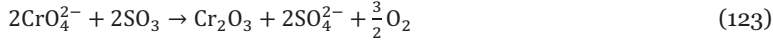
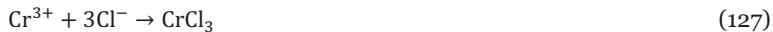


Figure 14. Predominance area phase diagrams of the Cr-S-O, Fe-S-O, Ni-S-O, Cr-Cl-O, Fe-Cl-O and Ni-Cl-O systems at 300 °C calculated by FactSage software version 7.3 using FactPS database.

During the corrosion experiments a mixed $\text{Cr}_2\text{O}_3 + \text{CrCl}_3$ scale was formed adjacent to the steel surface by reactions (126) and (127) below the Cr_2O_3 oxide at the temperature range of 300 °C – 350 °C.



At 250 °C, where the thick sulphate scale of iron, zinc and copper did not cover the steel surface, iron rich $(\text{Fe,Cr})_2\text{O}_3$ oxide was often formed. Even large internal corrosion damage composed of $\text{FeCl}_2/\text{FeCl}_3$ was detected. Otherwise, chlorides of chromium or nickel were not observed on the steel surface at 250 °C. The Gibbs energy change of CrCl_3 formation at 300 °C is -424,6 kJ/mol whereas for FeCl_2 it is -271,2 kJ/mol [86].

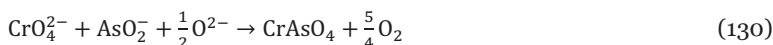
This means that chromium chloride should form in preference to iron chloride. However, CrCl_3 was not found near the iron chloride pitting corrosion. This in addition to low concentrations of chromium in the $(\text{Fe,Cr})_2\text{O}_3$ scale suggests that some chromium may have been lost in the form of gaseous chromium oxychlorides that could have formed according to reactions (127) and (128).



The atmosphere inside the furnace containing SO_2 , SO_3 and H_2SO_4 , stabilizes the sulphate scale consisting of ZnSO_4 , CuSO_4 , PbSO_4 and $\text{Fe}_2(\text{SO}_4)_3$ covering the mixed oxide and chloride scales on the steel surface, which successfully prevented formation of chromates (ZnCrO_4 , CuCrO_4 etc.), a highly destructive fluxing of Cr_2O_3 scales. [35, 38, 40, 41, 43, 48, 73, 87] Where the sulphate scale was thick and dense, it also prevented chromium vaporisation and instead, $\text{CrCl}_3/\text{Cr}_2\text{O}_3$ scale was found beneath the sulphate scale.

Chromium was not typically found in high concentrations within the sulphate layer covering the scale. However, as an exception to this, sometimes concentrations of over 10 wt% of chromium were detected together with the localized oxide structures containing high arsenic concentrations, possibly $\text{FeAsO}_4/\text{Fe}_3(\text{AsO}_4)_2$. Due to the small size of these arsenic enriched oxide areas, it is difficult to know which compounds they consist of, but according to FactSage calculations, they may be $\text{FeAsO}_4/\text{Fe}_3(\text{AsO}_4)_2$ and CrAsO_4 or $(\text{Fe,Cr})\text{AsO}_4$.

Since arsenic does not form sulphate in the temperature range of this study, the following assumption could be made regarding how chromium has ended up in the arsenic enriched oxide structure. If arsenic oxide would exhibit basic dissolution, similar to oxides of chromium and iron according to reaction (129), negative chromate solubility gradient could be formed due to local change in melt acidity. Arsenic chromate may be formed according to reaction (130) by reduction of chromate ions and oxidation arsenite ions. Arsenic oxides in the molten dust layer would have negative effect for the corrosion resistance of the stainless steels due to depleting the steel from chromium.



It is less likely that chromium would have been transported to react with the arsenic oxide in the sulphate layer of the scale in the form of CrCl_3 or $\text{Cr}_2\text{O}_2\text{Cl}_2$ since the solubility of chromium chloride in the sulphate melt was small in general. Development of the scale formed on the AISI 304 surface at 250 °C - 350 °C under copper smelter flue dust deposit is shown in Figure 15.

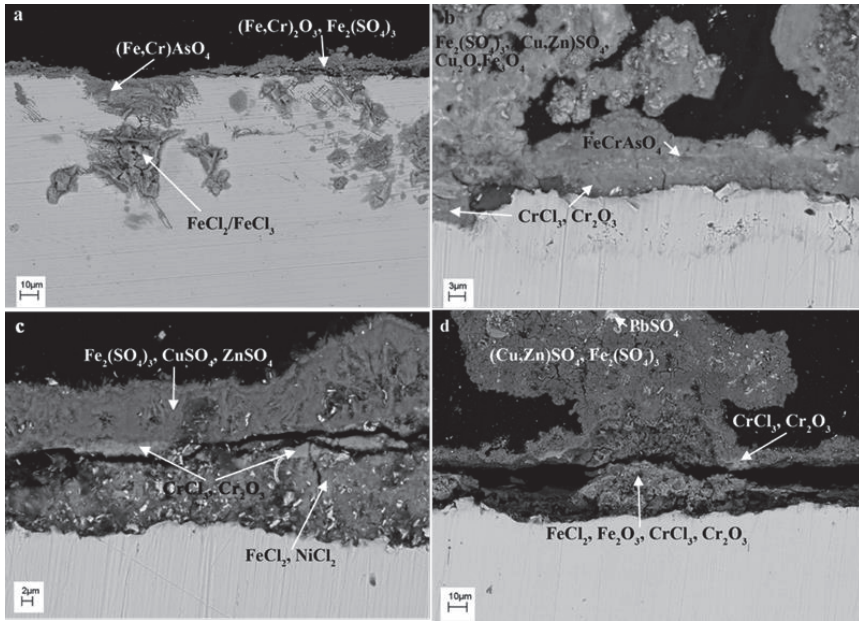


Figure 15. Pictures a-d represent scanning electron microscope images of cross-sections of the corroded surface of AISI 304 steel covered by deposit containing 65 wt% of copper smelter flue dust with 5 wt% KCl and 30 wt% ZnCl_2 after two weeks of exposure in 43 vol% SO_2 , 39 vol% N_2 , 9 vol% O_2 and 9 vol% H_2O atmosphere. Figure a represents corrosion reactions at 250 °C, b at 300 °C and c and d at 350 °C.

6.4 Corrosion resistance of AISI 316: The effect of Molybdenum alloying in the conditions of the heat recovery boiler

AISI 316 steel has similar chromium and nickel concentrations as AISI 304, but it also contains molybdenum as an alloying element. At 250 °C, the steel surface was unaffected by the molten deposit contrary to AISI 304, which suffered from internal corrosion. Only small concentration of steel's alloying elements were measured within the molten sulphate and no oxide formation or pitting corrosion was found anywhere in the sample. After rising of temperature to 300 °C, chlorides composed of the steels alloying metals started to form on the steel surface and the chloride scale grew in thickness rapidly when temperature was raised to 350 °C. Development of the scale formed on the AISI 316 surface at 250 °C – 350 °C under copper smelter flue dust deposit is shown in Figure 16.

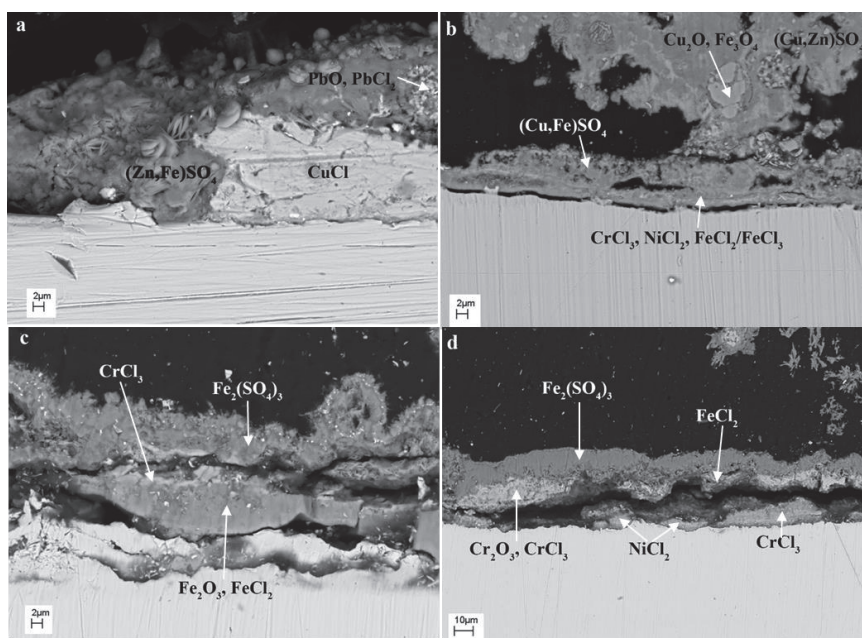


Figure 16. Pictures a-d represent scanning electron microscope images of cross-sections of the corroded surface of AISI 316 steel covered by deposit containing 65 wt% of copper smelter flue dust with 5 wt% KCl and 30 wt% ZnCl_2 after two weeks of exposure in 43 vol% SO_2 , 39 vol% N_2 , 9 vol% O_2 and 9 vol % H_2O atmosphere. Figure a represents corrosion reactions at 250 °C, b at 300 °C and c and d at 350 °C.

The beneficial effect of molybdenum alloying of stainless steels exposed to molten salt deposits has been reported in several occasions [35, 40, 41, 45]. Chromium, nickel and molybdenum accumulate on the steel surface beneath the oxide scale during high temperature exposure. Good corrosion protection of molybdenum alloyed steels is based on formation of a continuous protective MoO_2 oxide layer beneath the steels oxide scale lowering the dissolution rate of iron and other alloying elements in the oxide scale, thus maintaining the integrity of the protective Cr_2O_3 . [35, 40, 41, 45, 84]

Steels containing 3 - 4 % molybdenum are designed to withstand oxygen-free or reducing acid conditions [88]. The refractory metals, such as molybdenum, appear to have superior sulphidation resistance. The refractory metal sulphides are anion diffusers. For example, molybdenum sulphide has been shown to grow by inward sulphur transport. This means that, the large size of the sulphide anion has low mobility in the sulphide structure. Contrary to refractory metal sulphides, iron and nickel sulphides grow by outward cation transport resulting in fast sulphidation rates, since these transition metal sulphides have high cationic defect densities. The molybdenum sulphide is also closely stoichiometric, which acts as a barrier to outward diffusion of other alloy components. Even though the molybdenum sulphide slows the diffusion of other alloying elements through it, the alloy base metals are able to penetrate the molybdenum rich sulphides. The performance of molybdenum alloyed steels can be improved by addition of aluminum and manganese due to formation of double $\text{Al}_x\text{Mo}_2\text{S}_4$ and $\text{Mn}(\text{Fe})\text{S}$ as part of the inner scale layer, because aluminum and manganese sulphides are more stable than sulphides of Cr, Fe and Ni. Unfortunately, excessively high alloying levels

of Mo, Al, and Mn are required for practical engineering materials to achieve good protection against high sulphur potentials and even then, the benefit is limited by the extent to which the inner sulphide scale layers transmit other alloying metals, allowing growth of highly defective iron and nickel rich sulphides. [17]

The beneficial effect of molybdenum under chloride salts is based on the low vapour pressure of MoCl_4 , since the material loss is dependent on the vapour pressures of volatile species formed between the steels alloying metals and the corrosive environment. The difference between nickel and molybdenum is that nickel binds with two chlorine atoms whereas molybdenum reacts with chlorine to form higher coordinated compounds (MoCl_5) before it is stable enough to disengage from the steel surface. This requires higher chlorine partial pressures. [41]

6.5 Corrosion resistance of Sanicro 28: The effect of nickel alloying in the conditions of the heat recovery boiler

Superior oxidation resistance of high nickel stainless steels is partly due to low solubility of nickel in Cr_2O_3 . Iron has much larger solubility than nickel in Cr_2O_3 , which results in formation of a continuous, less protective FeCr_2O_4 scale. In order for MCr_2O_4 spinel structure to develop, metal cations (M^{n+}) need to diffuse outward in the Cr_2O_3 . Comparison of grain boundary diffusion coefficients of iron, chromium and nickel in Cr_2O_3 shows that the diffusion rate of nickel is the smallest, whereas iron and chromium have approximately the same diffusion rates [22]. Thus, increasing the Ni/Fe ratio decreases the steel's iron activity, which reduces iron solubility in Cr_2O_3 , retarding the FeCr_2O_4 formation. [29] Nickel may also decrease oxygen solubility or diffusivity in the steel. Decreasing oxygen solubility would have a similar effect as increasing chromium activity at the steel surface. [23]

Nickel alloying in stainless steels is also used to improve the steel's resistance to chlorination. The improved chlorination resistance of nickel containing alloys is based on the Gibbs energies of formation of chlorides. Chromium forms the most stable chloride of the steel's alloying metals and is for this reason most heavily attacked, whereas nickel chloride should start forming after iron and chromium are consumed, due to its smaller negative Gibbs energy of formation. The Gibbs energy changes of formation of chlorides, calculated by HSC version 8.1 are shown in Figure 17.

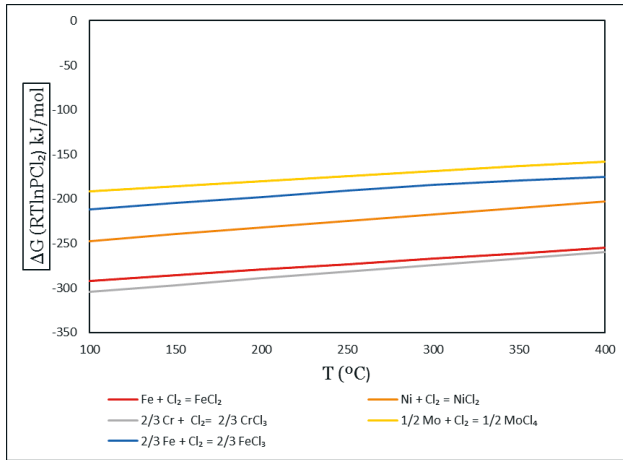


Figure 17. Gibbs energies of the chloride formation reactions of the steel's alloying metals calculated by HSC version 8.1 with MainDB8 database.

Based on visual observations, Sanicro 28 seemed to resist chlorination of the steel surface better compared to AISI 304 and AISI 316. At 250 °C, similar to AISI 304 and AISI 316, chlorides of the steel's alloying metals were not observed on the steel surface and at 300 °C, the extent of steel surface chlorination was modest. Only at 350 °C, thick chloride scales covered the steel surface in many locations.

Contrary to other stainless steels tested, high chromium and nickel concentrations were often found in the sulphate deposit of Sanicro 28 at the temperature range of 250 °C – 350 °C. Also, NiO precipitates were occasionally found within the molten dust deposit. NiSO₄, Cr₂(SO₄)₃ and NiO formation within the molten sulphate deposit may be a result of basic dissolution of NiCl₂ in the melt according to reactions (131) - (135) [30].



However, the fact that the same sulphate deposit containing mainly ZnSO₄, CuSO₄, FeSO₄ and PbSO₄ covered also AISI 304 and AISI 316 steels and all the studied steels developed similar chloride and oxide scales of chromium, iron and nickel below the sulphates, indicates that there is something different in the dissolution behaviour of the oxide scale of Sanicro 28. This was the only steel with extensive NiSO₄ and Cr₂(SO₄)₃ formation as corrosion products. Based on this, it is more likely that nickel and chromium sulphates have been formed by basic fluxing mechanism by molten sulphates involving NiO₂²⁻ and CrO₄²⁻ formation and their precipitation as Cr₂(SO₄)₃, NiSO₄ and NiO according to reactions (136) – (139).





Oxide dissolution rate, solubility in the melt and properties of the dissolution products determine the corrosion resistance of steels. Molten sulphates are reported to be especially aggressive towards high-nickel steels [89] due to synergistic dissolution behaviour of NiO and Cr₂O₃. In case of oxide film consisting of two different oxides, the more basic oxide should release oxide ions as a corrosion product thus exhibiting acidic dissolution according to reaction (140). Meanwhile, the acidic oxide reacts with those oxide ions resulting in basic dissolution in the salt layer according to reaction (141). The dissolution behaviour of the two oxides supports each other and consequently fluxing of the oxide scale proceeds faster compared to the situation where only either one of the oxides would be present. The dissolution kinetics of Cr₂O₃ becomes faster when combined with Fe₂O₃ and even higher kinetics is established in the presence of very basic oxides such as NiO combined with acidic oxide such as Cr₂O₃. [29] Development of the scale formed on the Sanicro 28 surface under copper smelter flue dust deposit is shown in Figure 18.

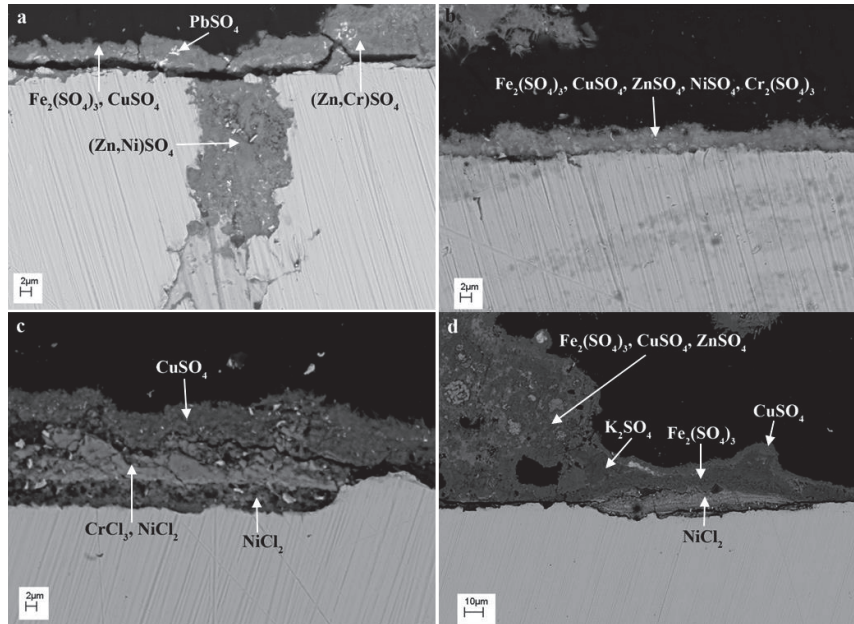
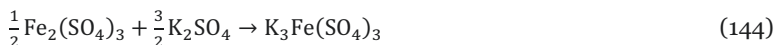
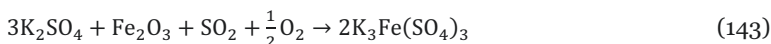


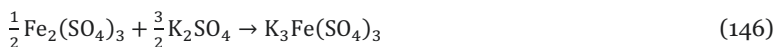
Figure 18. Pictures a-d represent scanning electron microscope images of cross-sections of the corroded surface of Sanicro 28 steel covered by deposit containing 65 wt% of copper smelter flue dust with 5 wt% KCl and 30 wt% ZnCl₂ after two weeks of exposure in 43 vol% SO₂, 39 vol% N₂, 9 vol% O₂ and 9 vol % H₂O atmosphere. Figure a represents corrosion reactions at 250 °C, b at 300 °C and c and d at 350 °C.

6.6 Sulphuric acid induced corrosion

The heat recovery boiler stainless steels used for cladding the carbon steel tubes were also exposed to the copper smelter off gas and the flue dust deposit without the addition of ZnCl_2 in the temperature range $250\text{ }^\circ\text{C} - 350\text{ }^\circ\text{C}$. These samples were used as references to compare the effect of heavy metal chlorides on the corrosion reactions of steel. The steel surfaces did not seem to react with the deposit or with the gas atmosphere except for the few locations where $\text{K}_3\text{Fe}(\text{SO}_4)_3$ was found on the steel surface. These areas were found on the surfaces of all of the studied steels at $250\text{ }^\circ\text{C} - 300\text{ }^\circ\text{C}$, but not at the highest experimental temperature. The steels showed no signs of corrosion at $350\text{ }^\circ\text{C}$. It seems KCl in the deposit is reactive with the steel surface and reacts to K_2SO_4 according to reaction (142). Chlorine was not measured anywhere on the steel surface. In absence of molten sulphate scale chlorine may have been lost to the flowing gas. $\text{K}_3\text{Fe}(\text{SO}_4)_3$ may have been formed according to reactions (143) – (144).



As discussed previously, the higher the temperature of the walls of the heat recovery boiler, the faster the corrosion rates. However, when SO_3 and H_2O coexist in the boiler atmosphere, liquid sulphuric acid (H_2SO_4) may form and cause low temperature corrosion by acidic fluxing of the steel's oxide if the dew point temperature is reached. [5] It is also possible that $\text{K}_3\text{Fe}(\text{SO}_4)_3$ formation on the steel surface can be explained by sulphuric acid condensation according to reactions (145) and (146) and acidic fluxing of Fe_2O_3 , where the Cr_2O_3 has been broken by chlorine. When molten sulphates covered the steel surfaces, sulphuric acid condensation would have been difficult to differentiate from the other sulphates.



SO_2 to SO_3 conversion fractions of 1-3 % have been estimated in the heat recovery boiler [3, 9]. The conversion rate of SO_2 to SO_3 is dependent on the partial pressures of SO_2 , O_2 and H_2O in the gas, the temperature and the chemical composition of flue dust, which acts as a catalyst for the oxidation of SO_2 to SO_3 . Increasing SO_2 and O_2 partial pressures in the gas increases the conversion rate of SO_2 to SO_3 up to a certain point after which the conversion rate decreases again. [10] The amount of SO_2 oxidized to SO_3 is significant, because the SO_3 and H_2O concentrations in the gas determine the dew point temperature of the sulphuric acid. The relationship between the SO_3 and H_2O concentration on the dew point temperature of H_2SO_4 is difficult to determine accurately, since several empirical models exist in the literature in addition to neural network modelling etc. Few of them are given by equations (147) - (149) [7, 8, 90, 91].

$$T_{\text{dewpoint}} = \frac{1000}{2.276 - 0.02943 \cdot \ln(p_{\text{H}_2\text{O}}) - 0.0858 \cdot \ln(p_{\text{SO}_3}) + 0.0062 \cdot \ln(p_{\text{H}_2\text{O}}) \cdot \ln(p_{\text{SO}_3})} \quad (147)$$

$$T_{dewpoint} = 365.6905 + 11.9864 * \ln(pH_2O) + 4.70336 * \ln(pSO_3) + (0.446 * \ln(pSO_3) + 5.2572)^{2.19} \quad (148)$$

$$T_{dewpoint} = 150 + 11.664 * \ln(pSO_3) + 8.13281 * \ln(pH_2O) - 0.383226 * \ln(pSO_3) * \ln(pH_2O) \quad (149)$$

The dew point temperature of H_2SO_4 rises as SO_3 and H_2O concentrations in the gas increase [7, 8, 92, 93]. In the off-gas of the flash smelting furnace, the SO_2 and therefore SO_3 concentrations of the gas are both an order of magnitude higher (10000s ppm) compared to the SO_3 concentration ranges, for which the equations (147) - (149) are designed (up to 1000 ppm). Therefore, the dew points calculated based on these equations should be considered with caution. Rather, a new model would be needed, which considers high SO_3 concentrations.

Lehmusto et al. [94, 95] have measured the catalytic effects of copper smelter flue dust on the oxidation of SO_2 to SO_3 . They also discovered that the impact of CuO as a catalyst was remarkably greater compared to other catalytic oxides present in the copper smelter flue dust. They also measured larger concentrations (5.8 vol%) of SO_2 converted to SO_3 than the previously evaluated 1-3 vol% as a result of passing the copper smelter off-gas through the flue dust. Based on the measurements of Lehmusto et al. [94, 95] the calculated sulphuric acid dew point temperatures with equations (147) - (149) would vary between 210 °C – 246 °C with the H_2O concentration of 9 vol%. The calculated result is close to the temperature of the heat recovery boiler wall. Since the empirical equations of the sulphuric acid dew point temperature have not been optimized to fit the SO_3 -levels in the heat recovery boiler, it is possible that liquid H_2SO_4 droplets condense on the boiler walls at the lowest operating temperature of 250 °C depending on the pressure of water circulating in the boiler pipes.

6.7 Microstructural considerations in corrosion prevention

A slowly growing, thin and well adherent Cr_2O_3 scale has been proven to provide optimal high temperature corrosion resistance for steels exposed to atmospheres that are either oxidizing, sulphidizing, water vapour containing, as well as steels under salt deposits. In addition to alloying, engineering an optimal microstructure can provide further improvement to corrosion resistance. With high enough chromium alloying (18-20 wt%) Cr_2O_3 forms on the steel surface providing optimal corrosion protection. The danger however lies with too slowly forming Cr_2O_3 scale, which can lead to absorption of corrosive elements into the steel, changing the oxide scale towards less protective structures. To address this risk, the outward diffusion rate of chromium must be enhanced by providing fast diffusion paths. This is especially important at temperatures below 800 °C, when the chromium diffusion rates via the lattice vacancies are much slower than via short circuit diffusion paths, like grain boundaries, dislocation etc. [96, 97]. In this case, the rate of formation and the microstructure of a protective Cr_2O_3 scale becomes more dependent on the steels microstructure. This will be discussed in more detail in this section.

The purpose of the research, presented in more detail in Article 1, was to evaluate whether by reducing the grain size of the steel, the high temperature oxidation resistance of boilers, and formation of dense and intact Cr_2O_3 scale can be improved by reducing the steels grain size. Therefore, the oxidation behaviour of austenitic TP347H steel with two grain sizes (9.1 ASTM and 5.1 ASTM) was studied.

In the initial stage of the oxidation process of TP347H steels, a thin protective Cr_2O_3 oxide scale is formed on the alloy steel surface. Manganese oxide is soluble in Cr_2O_3 and Mn^{4+} diffuses rapidly through the Cr_2O_3 via lattice sites rather than along the grain boundaries, and a chromium rich spinel with doped manganese oxide (MnCr_2O_4) is eventually formed. [17, 22]

In the case of thin oxide films, growth stresses arise from an epitaxial misfit caused by the differences between the lattice parameters of oxide and metal. As the oxide thickens, the epitaxial stresses become less significant and the main source of growth stresses is shifted towards the stresses formed by changes in the oxide composition. [13, 24] As Cr_2O_3 undergoes a phase transition from pure chromia to a spinel structure, the increase in molar volume is the main source of compressive stress in the scale. As a result, micro cracks are induced through which gaseous oxygen comes in direct contact with the chromium depleted steel surface. As the protective Cr_2O_3 oxide forms on the steel surface, the steel surface adjacent to the oxide depletes of chromium and at the same time enriches of iron. Oxygen that comes in contact with the steel surface beneath the protective chromia scale through a micro crack nucleates an iron-rich oxide nodule that grows rapidly. Oxygen diffuses easily through the iron rich oxide nodule and the oxidation zone proceeds both inward and outward from the original steel surface, increasing the risk of failure of the superheater tube. [13, 24]

Also niobium forms small oxide clusters on the $(\text{Cr,Mn})_2\text{O}_3$ surface. It is likely that during high temperature exposure, some of the NbC carbides oxidize, decomposing to Nb and CO, enabling elemental niobium to diffuse along the oxide grain boundaries and to form oxide clusters at the scale surface reducing its protectiveness. [98, 99] It seems that these clusters enhance the formation of some breakaway nodules by inducing cracks in the scale. Figure 19 shows the oxidized surface of TP347H steel. The cracking of the oxide due to the growth stresses may not be avoided, but the key to achieving good corrosion resistance is to ensure efficient maintenance of the growing oxide by quick supply of chromium to the steel surface.

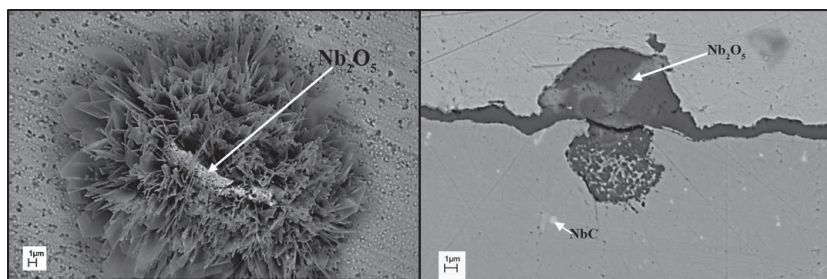


Figure 19. Iron enriched $(\text{Cr,Fe})_2\text{O}_3$ nodules found on the surfaces of TP347H steel oxidized at 600 °C and a cross section of an example of a $(\text{Cr,Fe})_2\text{O}_3$ nodule. The oxide surrounding the nodule is $(\text{Cr,Mn})_2\text{O}_3$.

Development of the oxidized coarse and fine-grained TP347H steel surface as a function of temperature (Figure 20) shows how significantly a higher grain boundary density speeds up the chromium supply, since the alloy grain boundaries serve as fast diffusion paths [100, 27]. Due to faster chromium mobility at 700 °C, a considerably smaller amount of nodules were formed on the steel surfaces. At 750 °C, the iron-rich breakaway nodules disappeared completely. This means that the critical chromium concentration tends to decrease with increasing temperature, because of the higher mobility of chromium in the steel, enabling it to reach the surface, heal and recover the uniform protective scale. When grain boundaries are further from each other, the chromium supply towards the centre of the grain is slower and iron oxides have time to grow before the healing Cr_2O_3 scale can form. Usually the iron enriched nodules grow in the middle of the grains. However, the nodules found together with niobium enriched oxide have probably grown on the grain boundary surface, since the NbC precipitates are located at the grain boundaries.

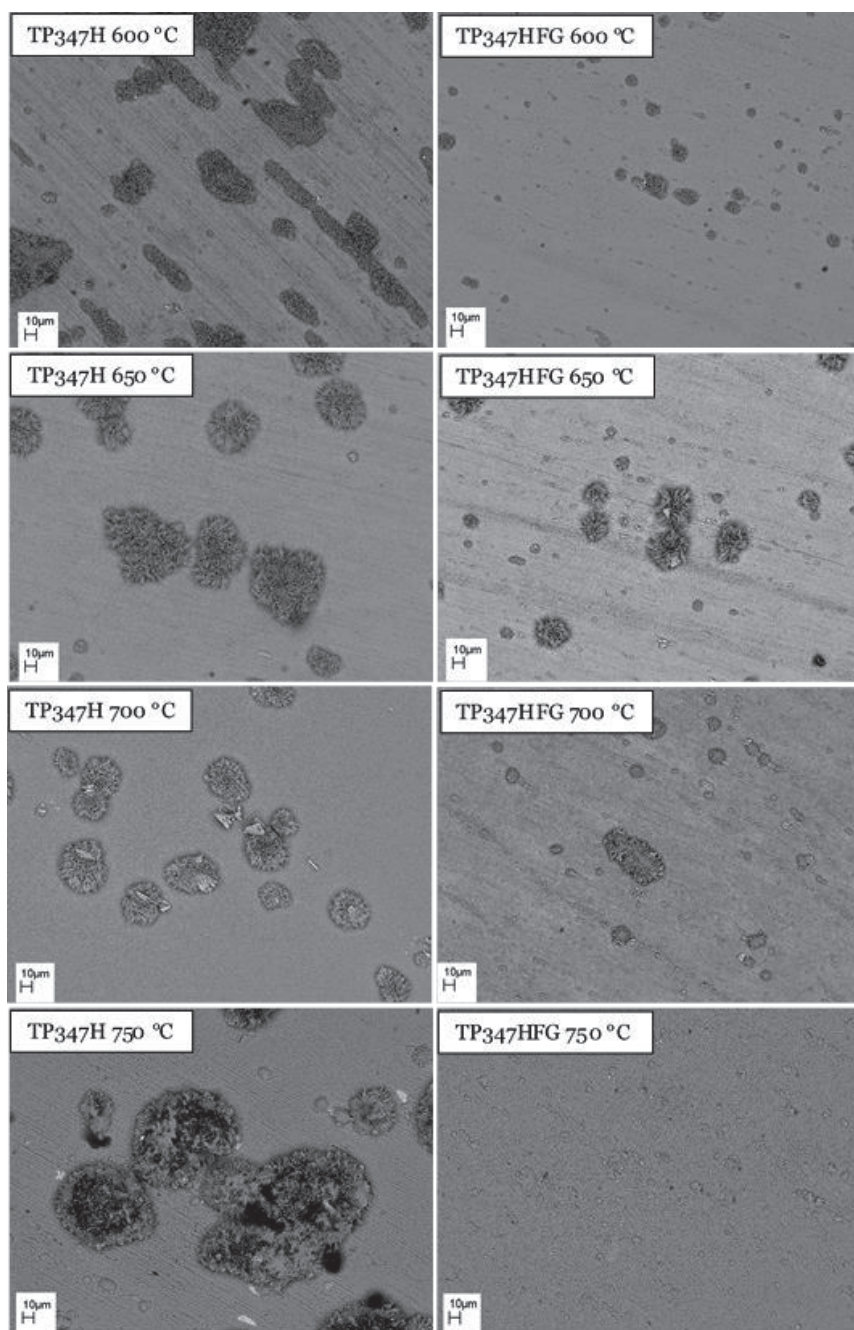


Figure 20. General views of the TP347H and TP347HFG surfaces after oxidation at temperatures 600 - 750 °C.

At 700 – 750 °C, chromium depletion of the steel surface becomes more pronounced, because of thicker scale formation. The chromium concentration below the scale at 750 °C was reduced to 11 wt% in the case of coarse-grained TP347H steel, which is not enough to prevent iron oxidation through a microcrack. TP347H type steel con-

tains 17 – 18 wt% of chromium which is considered as the minimum chromium concentration for protective continuous chromium oxide formation [11, 18]. In case of the coarse grained steel, enhanced mobility of chromium at higher temperature towards the steel surface was not fast enough to provide sufficient amount of chromium to prevent the formation of breakaway nodules.

Kinetic restrictions of the chromium supply due to low temperature in combination with cracking of the oxide scale at 600 – 650 °C result in too slow chromium flux from the bulk alloy towards the steel surface. Therefore, iron-rich breakaway nodules are formed also on the fine-grained steel surface at the lower experimental temperatures. As oxygen comes in contact with the steel surface through a micro-crack, the chromium will not reach the gas-steel boundary in time and an iron-rich oxide nodule nucleates instead. However, at 600 – 650 °C the oxide scale was so thin that the chromium depletion was not as severe as at higher temperatures. As a result, the Cr_2O_3 healing layer was formed after a while, stopping the oxidation process. This can be seen from the weight gain curves of the TP347H steels obtained during the initial oxidation at 600 – 750 °C shown in Figure 21. Activation energy for chromium diffusion in coarse grained steel was calculated to be 235 KJ/mol, while the activation energy for chromium diffusion in fine grained steel was calculated to be 145 KJ/mol, demonstrating how much more efficient diffusion along the grain boundaries is.

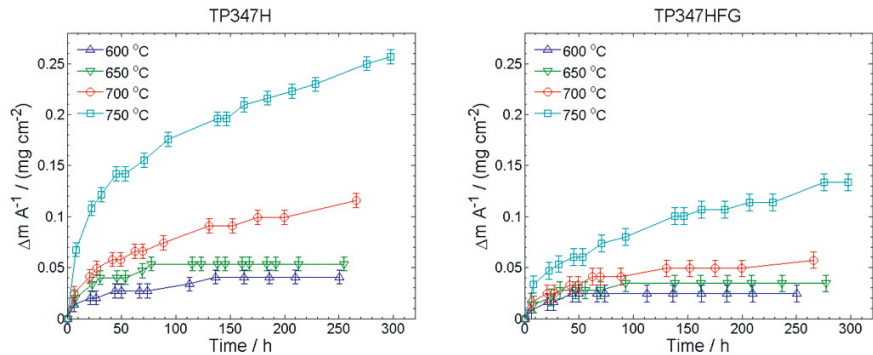


Figure 21. Initial oxidation kinetics of the TP347H steel with grain sizes 5.5 and 9.1 ASTM at 600 – 750 °C.

The fine grain structure of steel enhances oxide scale plasticity, enabling it to relieve high stresses and increase its adherence. Grain boundaries are known to act as nucleation sites for chromia, and therefore they will also promote the formation of finer grained and adherent scale thus reducing cracking. [25, 28]

7. Conclusions

Production of copper in the flash smelting process produces exceptionally high quantities of SO_2 gas, because copper is extracted by oxidizing sulphidic copper ores in a 1300°C flash smelting furnace. In addition to the SO_2 -rich, oxidizing gas, the ores contain various impurities, that vaporize and produce chemically complex dust. This aggressive cocktail of gas and dust is cleaned in a gas train, which involves removing the majority of dust from the off gas and collecting the process heat in the heat recovery boiler. The heat recovery boiler is a demanding environment for its steel pipe walls and the aim of this thesis was to discover the corrosion mechanism of the boiler among various possible chemical reactions between the steels, copper smelter flue dust and the off-gas.

Oxide particles from the ore end up in the heat recovery boiler in form of the dust, which is made to react to sulphates in the radiation section of the boiler. If the sulphation reactions are not complete, the dust particles contain oxide cores that are surrounded by sulphate surfaces. Often the dust also contains some chlorine originating from the ore. We found that within these oxide-, sulphate- and chloride-compounds that tend to stick on the boiler walls forming accretions the sulphation of the chlorides releases chlorine gas. The chlorine reacts easily with ZnO , PbO and Cu_2O to ZnCl_2 , PbCl_2 and CuCl . These reactions are detrimental, because the formation of these chlorides causes the dust deposit to melt at the operating temperature range ($250^\circ\text{C} - 350^\circ\text{C}$) of the heat recovery boiler walls. Molten salts, whether they are chlorides or sulphates dissolve the steel's protective oxide scales by fast electrochemical attack.

The extent of the melting of the dust deposit increases with increasing temperature resulting in faster corrosion. However, lowering the temperature of the boiler walls may not be optimal for the corrosion resistance either. H_2O and SO_3 gases in the boiler and within the dust deposit form H_2SO_4 . The oxides in the copper smelter flue dust have the strongest catalytic effect on the oxidation of SO_2 to SO_3 . It is likely that the extent of SO_3 formation is high enough to increase the sulphuric acid dew point temperature to the lower operating temperatures of the boiler walls, to around 250°C .

Finding an optimal steel for the boiler can help to increase the lifetime and cost efficiency of the copper flash smelting process. Corrosion resistant steels are alloyed with large enough concentrations of chromium, nickel, molybdenum and silicon. Thin, dense, adherent and quickly healing Cr_2O_3 scale formed on the steel surface provides optimal protection to all types of corrosion in the heat recovery boiler. The role of other alloying elements of steel is to maintain and promote the optimal Cr_2O_3 formation. If the alloying elements on the steel surface are consumed by the corrosive environment, the structure of Cr_2O_3 scale begins to deteriorate. Therefore, optimal stability of the

steels alloying metals in the corrosive environment increases the lifetime of the Cr_2O_3 scale.

In this thesis, three high alloy steels were studied in terms of their corrosion resistance in the conditions of the heat recovery boiler focusing on the role of chromium, nickel and molybdenum as alloying elements. AISI 304 and AISI 316 are similar high chromium steels, but AISI 316 is alloyed also with molybdenum. Sanicro 28 is a high chromium and high nickel steel and was studied to determine the importance of nickel alloying.

At 250 °C, chlorine induced corrosion of the studied steels was modest, despite the partial melting of the copper smelter flue dust. CrCl_3 , NiCl_2 , FeCl_2 and FeCl_3 scales started to develop on the steel surfaces at 300 °C and growing rapidly in thickness at 350 °C. Chlorine induced active oxidation of the steel surfaces was modest under the thick and dense molten sulphate layers based on the low concentrations of chromium and nickel in the molten sulphate deposit covering AISI 304 and AISI 316. Differences between the corrosion resistance of AISI 316 and AISI 304 were observed at 250 °C. At this temperature AISI 304 suffered rather extensive local internal corrosion damage, while the molybdenum alloying protected AISI 316, which did not show extensive signs of corrosion damage. High nickel Sanicro 28 was the only high alloy steel studied suffering from hot corrosion damage by basic fluxing mechanism of its oxide scale under molten sulphates, since high concentrations of nickel and chromium in the molten sulphate layer indicate formation of NiSO_4 , NiO and $\text{Cr}_2(\text{SO}_4)_3$ as corrosion products. Combination of Cr_2O_3 and NiO in the oxide scale results in increased oxide dissolution rates in the molten sulphate due to synergistic effects that the dissolution of these oxides have on each other during basic fluxing mechanism.

Chlorides are responsible for the corrosion damage of the heat recovery boiler because their presence in the dust deposit results in formation of molten salt mixtures and causes the chlorination of the steels. Therefore, it is necessary to avoid them in the feed mixture of the flash furnace. If chlorine contamination cannot be avoided, complete sulphation of the oxide containing dust may help to reduce the extent of melting when CuCl , ZnCl_2 and PbCl_2 formation from their oxides would be prevented. From the studied steels, AISI 316 seemed to be the most corrosion resistant option to be used in the conditions of the heat recovery boiler. In addition to alloying, reducing the steel grain size may be beneficial for the corrosion resistance especially at low temperature applications when diffusion of chromium in the steel takes place via short circuit diffusion paths such as grain boundaries. Large grain boundary density promotes the formation of fine grained and adherent Cr_2O_3 scale thus reducing oxide cracking.

References

- [1] W.G Davenport, M. King, M. Schlesinger, A.K. Biswas, Extractive Metallurgy of Copper, Fourth Edition, Pergamon, Kidlington Oxford (2002) 73-88, 217-246.
- [2] E. Miettinen, Thermal conductivity and characteristics of copper flash smelting flue dust accretions, *Doctoral thesis*, Helsinki University of Technology (2008), 1-38.
- [3] T. Ranki-Kilpinen, Sulphation of Cuprous and Cupric Oxide Dusts and Heterogeneous Copper Matte Particles In Simulated Flash Smelting Heat Recovery Boiler Conditions, *Doctoral thesis*, Helsinki University of Technology, Department of Materials Science and Rock Engineering (2004) 1-62.
- [4] T. Ahokainen, E. Peuraniemi, A. Jokilaakso, Experimental and computer simulation of gas-solid reactions in the flash smelting process, Technology Programme SULA 2, Energy in Steel and Base Metal Production (1998) 157 – 170.
- [5] D. Fleig, K. Andersson, F. Normann, F. Johnsson: 'SO₃ Formation under Oxyfuel Combustion Conditions', *Ind. Eng. Chem. Res.*, **50** (2011) 8505 – 8514.
- [6] R.K. Srivastava, C.A. Miller, C. Erickson, R. Jambhekar, Emissions of Sulphur Trioxide from Coal-Fired Power Plants, *Journal of the Air and Waste Management Association (JA&WMA)*, **54** (2004) 750 – 762.
- [7] B. ZareNezhad, A. Aminian, A multi-layer feed forward neural network model for accurate prediction of flue gas sulphuric acid dew points in process industries, *Appl. Therm. Eng.*, **30** (2010) 692 – 696.
- [8] J.M. Blanco, F. Pena, Increase in the boilers performance in terms of the acid dew point temperature: Environmental advantages of replacing fuels, *Appl. Therm. Eng.*, **28** (2008) 777 – 784.
- [9] S. Sarkar, Effect of SO₃ on Corrosion of Process Equipment in Copper Smelters, *JOM*, October (1982) 43-46.
- [10] L.P. Belo, L.K. Elliot, R.J. Stanger, R. Spörl, K.V. Shah, J. Meier, T.F. Wall: 'High-Temperature Conversion, of SO₂ to SO₃: Homogenous Experiments and Catalytic Effect of Fly Ash from Air and Oxy-fuel Firing', *Energy Fuels.*, **28** (2014) 7243 – 7251.
- [11] F.H. Stott, F.I. Wei, High Temperature oxidation of commercial austenitic stainless steels, *Mater. Sci. Technol.*, **5** (1989) 1140 – 1147.
- [12] G.Y. Lai, High Temperature Corrosion and Materials Applications, ASM International. (2007) 6 – 11, 226 – 230.
- [13] M. Schutze, Protective Oxide Scales and Their Breakdown, The Institute of Corrosion and Wiley Series on Corrosion and Protection, ISBN 0-471-95904 9 (1991) 2 – 37.
- [14] S.R.J. Saunders, M. Monteiro, F. Rizzo, The oxidation behavior of metals and alloys at high temperatures in atmospheres containing water vapour: A review, *Prog. Mater. Sci.*, **53** (2008) 775 – 873.
- [15] K.R. Trethewey, J. Chamberlain, Corrosion for Science and Engineering, 2. edition, Longman Group, (1995) 406 – 423.

- [16] N. Birks, G.H. Meier, Introduction to High Temperature Oxidation of Metals, (1983) 131 – 138.
- [17] D. Young, High Temperature oxidation and corrosion of Metals, Oxidation of Alloys, Corrosion by Sulphur, First Edition, Elsevier (2008) 185 – 243, 361 – 392.
- [18] S.N. Basu, G.J. Yurek, Effect of Alloy Grain Size and Silicon Content on the Oxidation of Austenitic Fe-Cr-Ni-Mn-Si Alloys in pure O₂, *Oxid. Met.*, **36** (1991) 281-315.
- [19] R. Viswanthan, J. Sarver, J.M. Tanzosh, Boiler Materials for Ultra-Supercritical Coal Power Plants – Steamside Oxidation, *J. Mater. Eng. Perform.*, **15** (2006) 255 – 273.
- [20] D.J. Young, B. Gleeson, Alloy phase transformations driven by high temperature corrosion processes, *Corros. Sci.* **44** (2002) 345 – 357.
- [21] F. Tholence, M. Norell, High Temperature Corrosion of Cast Alloys in Exhaust Environments. II-Cast Stainless Steels, *Oxid. Met.*, **69** (2008) 37 – 62.
- [22] R.E. Lobnig, H.P. Schmidt, K. Hennesen, H.J. Grabke, Diffusion of Cations in Chromia Layers Grown on Iron-Base Alloys, *Oxid. Met.*, **37** (1992) 81 – 93.
- [23] R. Peraldi, B.A. Pint, Effect of Cr and Ni Contents on the Oxidation Behavior of Ferritic and Austenitic Model Alloys in Air with Water Vapor, *Oxid. Met.*, **61** (2004) 463 – 483.
- [24] X. Peng, J. Yan, Y. Zhou, F. Wang, Effect of grain refinement on the resistance of 304 stainless steel to breakaway oxidation in wet air, *Acta Materialia*, **53** (2005) 5079 – 5088.
- [25] H.J. Grabke, E.M. Muller-Lorenz, S. Strauss, E. Pippel, J. Woltersdorf, Effects of Grain Size, Cold Working and Surface Finish on the Metal-Dusting Resistance of Steels, *Oxid. Met.*, **50** (1998) 241-254.
- [26] J-H. Kim, B.K. Kim, D-I. Kim, P-P. Choi, D. Raabe, K-W. Yi, The role of grain boundaries in the initial oxidation behaviour of austenitic stainless steel containing alloyed Cu at 700 °C for advanced thermal power plant applications, *Corros. Sci.*, **96** (2015), 52-66.
- [27] V. Trindade, H.J. Christ, U. Krupp, Grain-Size Effects on the High-Temperature Oxidation Behaviour of Chromium Steels, *Oxid. Met.*, **73** (2010) 551 – 563.
- [28] V. Trindade, U. Krupp, B. Z. Hanjari, S. Yang, H.J. Christ, Effect of Alloy Grain Size on the High-Temperature Oxidation Behaviour of the Austenitic Steel TP 347, *Mater. Res.*, **8** (2005) 371 – 375.
- [29] R.A. Rapp, Hot corrosion of materials: a fluxing mechanism?, *Corros. Sci.*, **44** (2002) 209 – 221.
- [30] M. Spiegel: 'Influence of gas phase composition on the hot corrosion of steels and nickel-based alloys beneath a (Ca-Na-K)-sulfate mixture containing PbSO₄ and ZnSO₄', *Mater. Corros.*, **51** (2000) 303 – 312.
- [31] F. Falk, M. Menneken, C. Stephan-Scherb, Real-Time Observation of High-Temperature Gas corrosion in Dry and Wet SO₂-Containing Atmosphere, *JOM*, **71** (2019) 1560-1565.
- [32] D.A. Shores, B.P. Mohanty, Role of chlorides in hot corrosion of a cast Fe-Cr-Ni alloy. Part II: thermochemical model studies, *Corros. Sci.*, **46** (2004) 2909 – 2924.
- [33] A. Jalowicka, W. Nowak, D. Naumenko, L. Singheiser, W.J. Quadakkers, Effect of nickel base superalloy composition on oxidation resistance in SO₂ containing, high pO₂ environments, *Mater. Corros.*, **65** (2014) 178 – 187.
- [34] B.P. Mohanty, D.A. Shores, Role of chlorides in hot corrosion of a cast Fe-Cr-Ni alloy. Part I: Experimental studies, *Corros. Sci.*, **46** (2004) 2893 – 2907.

- [35] Tz. Tzvetkoff, J. Kolchakov, Mechanism of growth, composition and structure of oxide films formed on ferrous alloys in molten salt electrolytes – a review, *Mater. Chem. Phys.*, **87** (2004) 201 – 211.
- [36] S.C. Srivastava, K.M. Godiwalla, M.K. Banerjee, Review Fuel ash corrosion of boiler and superheater tubes, *J. Mater. Sci.*, **32** (1997) 835 – 849.
- [37] H.J. Grabke, E. Reese, M. Spiegel, The effects of chlorides, hydrogen chloride and Sulphur dioxide in the oxidation of steels below deposits, *Corros. Sci.*, **37** (1995) 1023 – 1043.
- [38] H.P. Nielsen, F.J. Frandsen, K. Dam-Johansen, L.L. Baxter, The implications of chlorine-associated corrosion on the operation of biomass-fired boilers, *Prog.in Energy Combust. Sci.*, **26** (2000) 283 – 298.
- [39] M.A. Uusitalo, P.M.J. Vuoristo, T.A. Mäntylä, High temperature corrosion of coatings and boiler steels below chlorine-containing salt deposits, *Corros. Sci.*, **46** (2004) 1311-1331.
- [40] M.C. Galez, J.T. Bauer, M. Schutze, M. Noguchi, C. Takatoh, H. Cho, The influence of copper in ash deposits on the corrosion of boiler tube alloys for waste-to-energy plants, *Mater. Corros.*, **63** (2012) 1 – 8.
- [41] M.C. Galetz, J.T. Bauer, M. Schutze, M. Noguchi, H. Cho, Resistance of Coatings for Boiler Components of Waste-to-Energy Plants to Salt Melts Containing Copper Compounds, *J. Therm. Spray Technol.*, **22** (2013) 828 – 837.
- [42] D. Bankiewicz, P. Yrjas, M. Hupa, High-temperature Corrosion of Superheater Tube Materials Exposed to Zinc Salts, *Energy Fuels*, **23** (2009) 3469 – 3474.
- [43] P. Viklund, A. Hjörnhede, P. Henderson, A. Stålenheim, R. Pettersson, Corrosion of superheater materials in waste-to-energy plant, *Fuel Process. Technol.*, **105** (2011) 106 – 112.
- [44] P. Viklund, H. Kassman, L.-E. Åmand, Deposit chemistry and initial corrosion during biomass combustion – The influence of excess O₂ and sulphate injection, *Mater. Corros.*, **66** (2015) 118-127.
- [45] Y. Kawahara, High temperature corrosion mechanisms and effect of alloying elements for materials used in waste incineration environment, *Corros. Sci.*, **44** (2002) 223 – 245.
- [46] A.Zahs, M. Spiegel, H.J. Grabke, Chloridation and oxidation of iron, chromium, nickel and their alloys in chloridizing and oxidizing atmospheres at 400 – 700 °C, *Corros. Sci.*, **42** (2000) 1093 – 1122.
- [47] A. Ruh, M. Spiegel, Thermodynamic and kinetic consideration on the corrosion of Fe, Ni and Cr beneath the molten KCl-ZnCl₂ mixture, *Corros. Sci.*, **48** (2006) 679 – 695.
- [48] J. Lehmusto, Doctoral thesis, The role of Potassium in the Corrosion of Superheater material in Boilers Firing Biomass, Åbo Akademi University (2013) 1 – 132.
- [49] P. Kofstad, High Temperature Oxidation of Metals, The Corrosion Monograph Series, John Wiley and Sons Inc, (1966), 10 – 19, 46
- [50] E.Haccuria, T. Grivits, P.C. Hayes, E. Jak, Selected Phase Equilibria Studies in the Al₂O₃-CaO-SiO₂ System, *J. Am. Ceram. Soc.* **99** (2016) 691-704.
- [51] E. Jak, Integrated experimental and thermodynamic modelling research methodology for metallurgical slags with examples in the copper production field, *Int.Symp.Molten*, Beijing, (2012) 1-21.
- [52] J.C. Zhao, J.F. Smith, Methods for Phase Diagram Determination, Introduction to phase diagrams, Elsevier Amsterdam, First Edition (2007) 10 – 13
- [53] A.F. Holleman, E. Wiberg, Inorganic Chemistry, Academic Press San Diego (2001), ISBN: 0123526515.

- [54] A.F. Wells, Structural Inorganic Chemistry, Oxford: Clarendon press (1984)
ISBN: 0198553706.
- [55] A.K. De, A Textbook of Inorganic Chemistry, 9th edition, New Age International (P) Ltd. Publishers, New Delhi (2003).
- [56] G. De Micco, D. M. Pasquevich, A. E. Bohé, Interactions during the chlorination of a copper–zinc alloy. *Thermochim. Acta*, **470** (2008) 83-90.
- [57] G. DeMicco, F.J. Alvarez, A.E. Bohe, D.M. Pasquevich, Chlorination applied to separation of metals, Sohn International Symposium Advanced Processing of Metals and Materials, New, Improved and existing technologies Iron and steel and recycling and waste treatment, *TMS* **5** (2006) 403 -418.
- [58] J.L. Pouchou and F. Pichoir, Advanced Quantitative Procedures for analytical SEM and EPMA: X-ray microanalysis of light elements and layered specimens, 10th European Congress on Electronic Microscopy (EUREM 92) (1992) 1 – 5.
- [59] N. Saunders, A.P. Miodownik, Calphad Calculation of Phase Diagrams: A Comprehensive guide, Thermodynamic models for solution and compound phases, Pergamon Materials Series, Cambridge (1998) 91 – 124.
- [60] M. Hillert, Phase Equilibria, Phase Diagrams and Phase Transformations, Their Thermodynamic Basis, Mathematical modelling of solution phases, Cambridge University Press, Cambridge (1998) 458 – 499.
- [61] H.S. Lukas, S.G. Fries, B. Sundman, Computational Thermodynamics, The Calphad Method, Models for the Gibbs energy, Cambridge University Press, New York, First edition (2007) 79 – 157.
- [62] D. Lindberg, Thermochemistry and melting properties of alkali salt mixtures in black liquor conversion processes, Doctoral Thesis, Åbo Akademi, Process Chemistry Centre, Laboratory of Inorganic Chemistry (2007) 9-26.
- [63] M. Hillert, The compound energy formalism, *J. Alloys and Compounds*, **320** (2001) 161-176.
- [64] K. Wang, C. Robelin, Z. Wu, C. Li, L. Xie, P. Chartrand, Thermodynamic description of the AgCl-CoCl₂-InCl₃-NaCl system, *J. Alloys and Compounds*, **663** (2016) 885 – 898.
- [65] A.D. Pelton, S.A. Degterov, G. Eriksson, C. Robelin, Y. Dessureault, The modified Quasichemical model 1 – Binary Solutions, *Metall. Mater. Trans. B*, **31B**, (2000) 651– 659.
- [66] A.D. Pelton, P. Chartrand, The modified Quasi-chemical model: Part II. Multi-component Solutions, *Metall. Mater. Trans. A*, **32A** (2001) 1355 – 1360.
- [67] P. Chartrand, A.D. Pelton, The Modified Quasi-chemical Model: Part III. Two sublattices, *Metall. Mater. Trans. A*, **32A** (2001) 1397-1407.
- [68] A.D. Pelton, P. Chartrand, G. Eriksson, The Modified Quasi-chemical model: Part IV. Two-Sublattice Quadruplet Approximation, *Metall. Mater. Trans. A*, **32A** (2001) 1409-1416.
- [69] C. Robelin, P. Chartrand, A.D. Pelton, Thermodynamic evaluation and optimization of the (MgCl₂ + CaCl₂ + MnCl₂ + FeCl₂ + CoCl₂ + NiCl₂) system, *J. Chem. Thermodynamics*, **36** (2004) 793 – 808.
- [70] C. Robelin, P. Chartrand, A.D. Pelton, Thermodynamic evaluation and optimization of the (NaCl + KCl + MgCl₂+ CaCl₂ + MnCl₂ + FeCl₂ + CoCl₂ + NiCl₂) system, *J. Chem. Thermodynamics*, **36** (2004) 809 – 828.
- [71] C. Robelin, P. Chartrand, Thermodynamic evaluation and optimization of the (NaCl + KCl + MgCl₂+ CaCl₂ + ZnCl₂) system, *J. Chem. Thermodynamics*, **43** (2011) 377 – 391.
- [72] B.-J. Skrifvars, R. Backman, M. Hupa, K. Salmenoja and E. Vakkilainen, *Corros. Sci.* **50** (2008) 1274 – 1282.

- [73] B.-J. Skrifvars, M. Westen-Karlsson, M. Hupa and K. Salmenoja, *Corros. Sci.* **52** (2010) 1011 – 1019.
- [74] G. Herrmann, Über die Verbindungsfähigkeit der Chloride von Cu, Pb, Fe, Zn, Sn und Bi, *Z. Anorg. Chem.* **71** (1911) 257 – 302.
- [75] A. P. Palkin, G. P. Chepurko, The reaction of salts with metals in the molten state. The reaction of CuCl with zinc, *Zh. Neorg. Khim.* **8** (1956) 1833-1842.
- [76] D. S. Coleman, P. D. A. Lacy, Phase equilibrium diagrams of the system calcium chloride-cuprous chloride-plumbous chloride. Inst. Mining Met., Trans. Sect. C, **77** (1968) C170-C173.
- [77] W. Biltzt, W. Fischer, Beiträge zur systematischen Verwandtschaftslehre über das System Cupro-/Cuprichlorid, Hannover, Technische Hochschule, Institut für anorganische Chemie. (1927) 290 -299.
- [78] V.V. Safonov, V.A. Mireiev, S.K. Dubina, D.V. Baiandin, *Z. Neorg. Chim.* **30** (1987) 2372.
- [79] V. H. Schäfer, L. Bayer, Das Zustandsdiagramm Eisen (III)-chlorid-Eisen (II)-chlorid, *Z. anorg. Allg. Chem.* **271** (1953) 338 – 346.
- [80] N. G. Korzhukov, Y. B. Kabonin, Melting diagrams of the FeCl₂-CuCl₂ and CoCl₂-CuCl₂ systems. Vestnik Moskovskogo Universiteta, Seriya 2: Khimiya, **21** (1966) 66-68.
- [81] A. Rahmel, Molten salt technology, 10. Corrosion, ed. D.G. Lovering, first edition, Plenum Press, New York (1982) 265 - 283.
- [82] T. Jonsson, N. Folkesson, M. Halvarsson, J.-E. Svensson and L.-G. Johansson, High-Temperature Oxidation of FeCr(Ni) Alloys: The Behaviour After Breakaway, *Oxid. Met.*, **81** (2014) 575 – 596.
- [83] D. Bankiewicz, E. Alonso-Herranz, P. Yrjas, T. Lauren, H. Spliethoff and M. Hupa, Role of ZnCl₂ in High-Temperature Corrosion in a Bench-Scale Fluidized Bed Firing Simulated Waste Wood Pellets, *Energy Fuels* **25** (2011) 3476 – 3483.
- [84] M.C. Galetz, B. Rammer and M. Schutze, Refractory metals and nickel in high temperature chlorine-containing environments - thermodynamic prediction of volatile corrosion products and surface reaction mechanisms: a review, *Mater. Corros.* **66** (2015) 1206 – 1214.
- [85] N. Otsuka and R.A. Rapp, Effects of Chromate and Vanadate Anions on the Hot Corrosion of Preoxidized Ni by a Thin Fused Na₂SO₄ Film at 900°C, *Journal of Electrochemical Society*, **137** (1990) 53 – 60.
- [86] Y.K. Rao, Stoichiometry and Thermodynamics of Metallurgical Processes, Cambridge University press. New York (1985) 880 – 894.
- [87] J. Sui, J. Lehmusto, M. Bergelin and M. Hupa, The Onset of Potassium Chloride Induced High Temperature Corrosion: A Novel Experimental Approach, *Oxid. Met.*, **82** (2014) 437 – 456.
- [88] D. Bankiewicz, P. Yrjas, D. Lindberg, M. Hupa, Determination of the corrosivity of Pb-containing salt mixtures, *Corros. Sci.*, **66** (2013) 225 – 232.
- [89] T. Tzvetkoff, P. Gencheva: 'Mechanism of formation of corrosion layers on nickel and nickel-based alloys in melts containing oxyanions – a review', *Mater. Chem. Phys.*, **82** (2003) 897 – 904.
- [90] F.H. Verhoff, J.T. Banchemo: 'Predicting dew points of flue gases', *Chem. Eng. Prog.*, **70** (1974) 71 – 72.
- [91] A.G. Okkes, Get acid dew point of flue gas, *Hydrocarb. Process*, **66** (1987) 53.
- [92] R.K. Srivastava, C.A. Miller, C. Erickson, R. Jambhekar, Emissions of Sulphur Trioxide from Coal-Fired Power Plants, *J. Air Waste Manage. Assoc.*, **54** (2004) 750 – 762.

- [93] V.M.M. Huijbregts, R.G.I. Leferink: ‘Latest advances in the understanding of acid dewpoint corrosion: corrosion and stress corrosion cracking in combustion gas condensates’, *Anti Corros. Method. M.*, 2004, 51, 173 – 188.
- [94] J. Lehmusto, E. Vainio, T. Lauren, M. Lindegren, The Effect of deposit temperature on the catalytic SO₂-to-SO₃ Conversion in a Copper Flash Smelting Heat Recovery Boiler, *Metallurgical and Materials Transactions B*, **49B** (2017) 434 – 439.
- [95] J. Lehmusto, T. Lauren, M. Lindegren, Catalytic Role of Process Dust in SO₂-to-SO₃ Conversion in Flash Smelting Heat Recovery Boilers, *JOM* **71** (2019) 3305 – 3313.
- [96] V. Linnenbom, M. Tetenbaum, C. Cheek, Tracer Diffusion of Iron in Stainless Steel, *J. Appl. Phys.*, **26** (1955) 932 – 936.
- [97] A. F. Smith, G.B. Gibbs, Volume and Grain-Boundary Diffusion in 20 Cr/25 Ni/Nb Stainless Steel, *Met. Sci. J.* **3** (1969) 93 – 94.
- [98] C. F. Miller, G. W. Simmons, R.P. Wei, High temperature oxidation of Nb, NbC and Ni₃Nb and oxygen enhanced crack growth, *Scripta mater*, **42** (2000) 227 – 232.
- [99] T. Moroishi, H. Fujikawa, H. Makiura, The Effect of Carbon, Zirconium, Niobium, and Titanium on the Oxidation Resistance of Chromium Stainless Steel, *J. Electrochem. Soc.*, **126** (1979) 2173 – 2182.
- [100] W.E. Boggs, The Oxidation of Iron-Aluminum Alloys from 450° to 900°C, *Solid State Sci.*, **118** (1971) 906-913.



ISBN 978-952-60-8929-4 (printed)

ISBN 978-952-60-8930-0 (pdf)

ISSN 1799-4934 (printed)

ISSN 1799-4942 (pdf)

Aalto University

School of Chemical Engineering

Department of Metallurgical and Chemical Engineering

www.aalto.fi

**BUSINESS +
ECONOMY**

**ART +
DESIGN +
ARCHITECTURE**

**SCIENCE +
TECHNOLOGY**

CROSSOVER

**DOCTORAL
DISSERTATIONS**